



TITLE:

Updated absolute gravity rate of change associated with glacial isostatic adjustment in Southeast Alaska and its utilization for rheological parameter estimation

AUTHOR(S):

Naganawa, Kazuhiro; Kazama, Takahito; Fukuda, Yoichi; Miura, Satoshi; Hayakawa, Hideaki; Ohta, Yusaku; Freymueller, Jeffrey T.

CITATION:

Naganawa, Kazuhiro ...[et al]. Updated absolute gravity rate of change associated with glacial isostatic adjustment in Southeast Alaska and its utilization for rheological parameter estimation. *Earth, Planets and Space* 2022, 74: 116.

ISSUE DATE:

2022

URL:

<http://hdl.handle.net/2433/277737>

RIGHT:

© The Author(s) 2022.; This article is licensed under a Creative Commons Attribution 4.0 International License, which permits use, sharing, adaptation, distribution and reproduction in any medium or format, as long as you give appropriate credit to the original author(s) and the source, provide a link to the Creative Commons licence, and indicate if changes were made. The images or other third party material in this article are included in the article's Creative Commons licence, unless indicated otherwise in a credit line to the material. If material is not included in the article's Creative Commons licence and your intended use is not permitted by statutory regulation or exceeds the permitted use, you will need to obtain permission directly from the copyright holder.

FULL PAPER

Open Access



Updated absolute gravity rate of change associated with glacial isostatic adjustment in Southeast Alaska and its utilization for rheological parameter estimation

Kazuhiro Naganawa^{1*} , Takahito Kazama¹, Yoichi Fukuda^{1,2}, Satoshi Miura³, Hideaki Hayakawa⁴, Yusaku Ohta³ and Jeffrey T. Freymueller^{5,6}

Abstract

In Southeast Alaska (SE-AK), rapid ground uplift of up to 3 cm/yr has been observed associated with post-Little Ice Age glacial isostatic adjustment (GIA). Geodetic techniques such as global navigation satellite system (GNSS) and absolute gravimetry have been applied to monitor GIA since the last 1990s. Rheological parameters for SE-AK were determined from dense GNSS array data in earlier studies. However, the absolute gravity rate of change observed in SE-AK was inconsistent with the ground uplift rate, mainly because few gravity measurements from 2006 to 2008 resulted in imprecise gravity variation rates. Therefore, we collected absolute gravity data at six gravity points in SE-AK every June in 2012, 2013, and 2015, and updated the gravity variation rate by reprocessing the absolute gravity data collected from 2006 to 2015. We found that the updated gravity variation rate at the six gravity points ranged from -2.05 to -4.40 $\mu\text{Gal}/\text{yr}$, and its standard deviation was smaller than that reported in the earlier study by up to 88 %. We also estimated the rheological parameters under the assumption of the incompressible Earth to explain the updated gravity variation rate, and their optimal values were determined to be 55 km and 1.2×10^{19} Pa s for lithospheric thickness and upper mantle viscosity, respectively. These optimal values are consistent with those independently obtained from GNSS observations, and this fact indicates that absolute gravimetry can be one of the most effective methods in determining sub-surface structural parameters associated with GIA accurately. Moreover, we utilized the gravity variation rates for estimating the ratio of gravity variation to vertical ground deformation at the six gravity points in SE-AK. The viscous ratio values were obtained as -0.168 and -0.171 $\mu\text{Gal}/\text{mm}$ from the observed data and the calculated result, respectively. These ratios are greater (in absolute) than those for other GIA regions (-0.15 to -0.16 $\mu\text{Gal}/\text{mm}$ in Antarctica and Fennoscandia), because glaciers in SE-AK have melted more recently than in other regions.

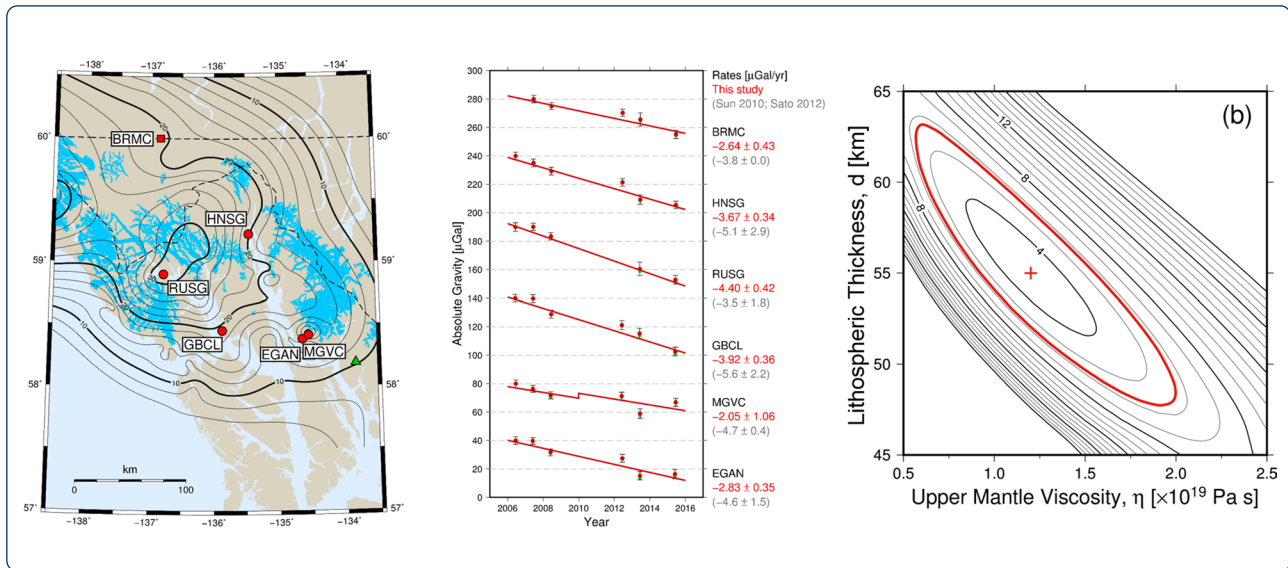
Keywords: Absolute gravity change, Southeast Alaska, Rheological parameter, Mantle viscosity, Lithospheric thickness, Present-day ice melting, Little Ice Age, Vertical gravity gradient

Graphical Abstract

*Correspondence: naganawa.kazuhiro.research@gmail.com

¹ Graduate School of Science, Kyoto University, Sakyo-ku, Kyoto 606-8502, Japan

Full list of author information is available at the end of the article



Introduction

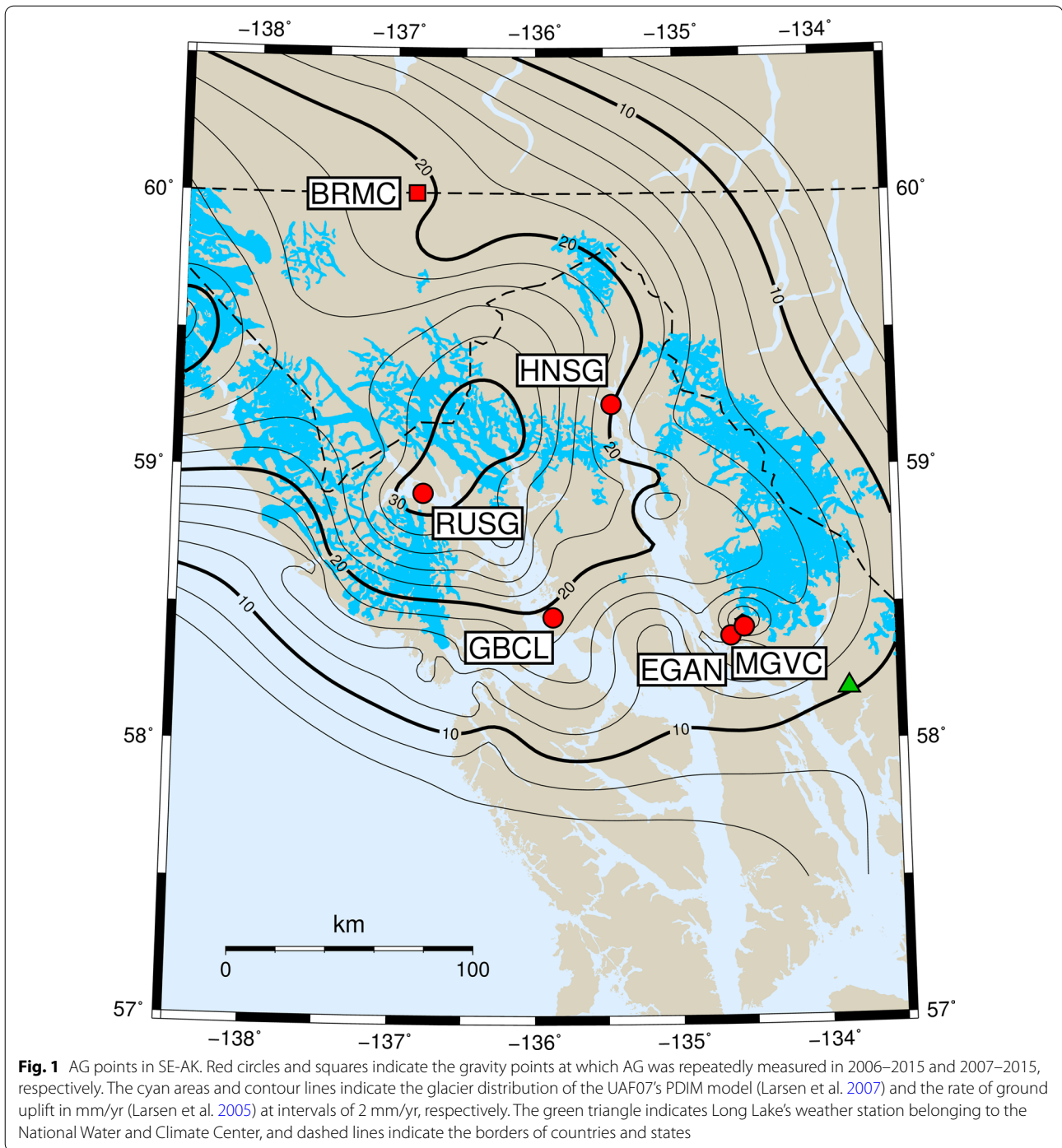
In Southeast Alaska (SE-AK), significant masses of glaciers have melted in the 19–20th centuries after the Little Ice Age (LIA), and the glacier melting is still ongoing. Rapid ground uplift of up to 3 cm/yr has been observed at the global navigation satellite system (GNSS) stations in this region (Fig. 1; Larsen et al. 2004), which is mainly caused by Glacial Isostatic Adjustment (GIA, i.e., the elastic/viscoelastic response of solid earth to present/past glacier mass changes). Since 1998, GNSS stations have been surveyed in SE-AK to determine the spatiotemporal variations in the uplift rate more precisely (Larsen et al. 2005). The observed uplift rates were quantitatively reproduced using GIA models, which are composed of spatiotemporal ice load distributions and medium parameters indicating a thin lithosphere (~ 60 km) and low-viscosity asthenosphere ($\sim 10^{19}$ Pa s) (Larsen et al. 2004, 2005; Elliott et al. 2010; Sato et al. 2011; Hu and Freymueller 2019).

Sun et al. (2010) also measured absolute gravity (AG) values on the ground in SE-AK every June from 2006 to 2008 as part of the International geodetic project in South-Eastern Alaska (ISEA) (fiscal years: 2005–2008) to reveal the spatiotemporal mass variations associated with GIA and present-day ice melting (PDIM) directly. They determined the AG at five gravity points (red circles in Fig. 1) within 1-μGal precision ($1 \mu\text{Gal} = 1 \times 10^{-8} \text{ m/s}^2$), and found a linear gravity decrease of up to $-5.6 \mu\text{Gal/yr}$. Sato et al. (2012) additionally determined the AG variation rate at Blanchard Road Maintenance Compound (BRMC) (red square in Fig. 1) to be $-2.9 \mu\text{Gal/yr}$ using AG data collected in June 2007 and 2008, and reproduced

the AG variation rates at six gravity points (red circles and squares in Fig. 1) using their GIA model (Sato et al. 2011).

However, the following three problems still exist for all the earlier studies on gravity variations in SE-AK (Sun et al. 2010; Sato et al. 2012). First, a 3-year duration is too short to obtain precise AG variation rates. In the earlier studies, 1-σ error values of the AG variation rates at five gravity points were estimated to be 0.4–2.9 μGal/yr, which corresponded to 9–57 % of the absolute values of the AG variation rates (Sun et al. 2010). If AG is newly measured at the same gravity points after an interval of several years, more precise variation rates can be obtained. Second, Sato et al. (2011, 2012) decreased the resolution of PDIM models (Larsen et al. 2005, 2007) on purpose to reduce the computational time. Since gravity change is sensitive to the spatiotemporal variation in ice melting, high-resolution PDIM models should be prepared to calculate gravity variations accurately. Third, none of the earlier studies have created GIA models from the AG variation rate itself; for example, Sato et al. (2012) simply reproduced the observed AG variation rate using their GIA model, which was based on the GNSS data (Sato et al. 2011). Although less AG data are available relative to the GNSS data, a new GIA model can be developed from the AG data given a longer AG time series, and it should be compared with earlier GNSS-based models (e.g., Sato et al. 2011; Hu and Freymueller 2019). It is also worthwhile to create GIA models from the AG variation rate, because gravity observations have the advantage that they are independent of the reference frame and its associated errors.

Thus, we construct a new GIA model using high-resolution PDIM models and an updated data set of AG observations from 2006 to 2015. New AG measurements



were collected at six gravity points in SE-AK every June in 2012, 2013, and 2015 as part of the ISEA2 project (fiscal years: 2011–2015), and all of the AG data from 2006 to 2015 are reprocessed using a consistent procedure. AG variation rates are obtained from the AG data set from 2006 to 2015 after correcting for hydrological and coseismic gravity changes, and the obtained AG variation rates

are quantitatively assessed by numerical calculations of gravity changes derived from GIA and PDIM. High-resolution PDIM models are then utilized, and optimal medium parameters such as lithospheric thickness and asthenospheric viscosity are determined. The coherency of the medium parameters is finally discussed by comparing the observed uplift rate with the one calculated

from our GIA model under the common assumption of the incompressible Earth.

Absolute gravity data

We conducted repeated AG measurements at six gravity points (red symbols in Fig. 1) in June 2012, 2013, and 2015 using an FG5 absolute gravimeter (serial number: 111) (Micro-g LaCoste 2006). Table 1 shows the coordinates and vertical gravity gradient of the AG points, along with coordinates of their nearest continuous GNSS stations. The FG5 gravimeter was set up at most of the AG points according to the Appendix in Sun et al. (2010). However, at Mendenhall Glacier Visitor Center (MGVC), we needed to move the AG point by about 5 m in June 2012, because an exhibit was installed on the old AG point by the visitor center (see Appendix A). The gravity difference between the old and new gravity points for MGVC was estimated with the least-square method, as discussed in the next section. The AG data were collected for approximately 2 days at each point to obtain approximately 100 sets of gravity values. One set was composed of 100 drops of the gravity measurement, and the set and drop intervals were chosen to be 30 min and 10 s, respectively.

The AG data were then processed using the g9 software (Micro-g LaCoste 2012) with basic gravity corrections applied to each gravity data as follows: the effect of air pressure change was corrected using the air pressure data simultaneously obtained by an internal barometer in the FG5's controller unit with an admittance factor of $-0.30 \mu\text{Gal}/\text{hPa}$ and nominal air pressure values, as shown in Table 1; the solid earth tide was corrected using the ETGTAB software (Timmen and Wenzel 1995) with the delta factor for permanent tide of 1.0; the polar motion effect was corrected using polar position values provided by International Earth Rotation and Reference Systems Service (IERS) Bulletin A and a delta factor of 1.164; the AG at a height of 100 cm from the benchmark of each gravity point was estimated through correction of the instrumental height difference using the gravity gradient values, as shown in Table 1. The ocean-tide loading effect was also corrected with the regional ocean-tide model developed by Inazu et al. (2009), but we found that diurnal and semidiurnal gravity changes persisted in the time series of gravity sets at seashore AG points (Fig. 2a) due to the under-correction of the ocean-tide effect. Although the ocean-tide model should be improved in future studies, we applied a regression of the diurnal and semidiurnal sine curves to the set gravity

Table 1 Parameters of AG points (Sun et al., 2010) and their nearest GNSS stations

<i>AG point</i>						
Name	EGAN	MGVC	GBCL	RUSG	HNSG	BRMC
Latitude [deg]	58.38534	58.41736	58.45462	58.90639	59.23186	60.00183
Longitude [deg]	-134.64002	-134.54617	-135.87488	-136.78908	-135.45977	-136.85511
Elevation [m]	38.0	8.0	21.0	10.0	21.0	840.0
Nominal air pressure [hPa]	1008.69	1012.29	1010.73	1012.05	1010.73	916.33
Gravity gradient [$\mu\text{Gal}/\text{cm}$]	-2.734	-2.045 ^a -2.364 ^b	-3.099	-3.468	-3.093	-2.910
Distance to nearest glacier ^c [km]	7.37	1.46	30.82	6.81	11.56	31.09
<i>Continuous GNSS station</i>						
Name	AB50	AB50	GUS0 ^d	QUIC	AB44	MDFC
Data analyst	UNAVCO	UNAVCO	UNAVCO	NGL ^e	UNAVCO	NGL
Latitude [deg]	58.41678	58.41678	58.41776	58.90856	59.52804	60.12182
Longitude [deg]	-134.54530	-134.54530	-135.69705	-136.58682	-135.22830	-136.95833
Ellipsoidal height [m]	51.6	51.6	19.9	23.8	304.2	897.0
Distance from AG point [km]	6.53	0.08	11.13	11.61	35.42	14.51

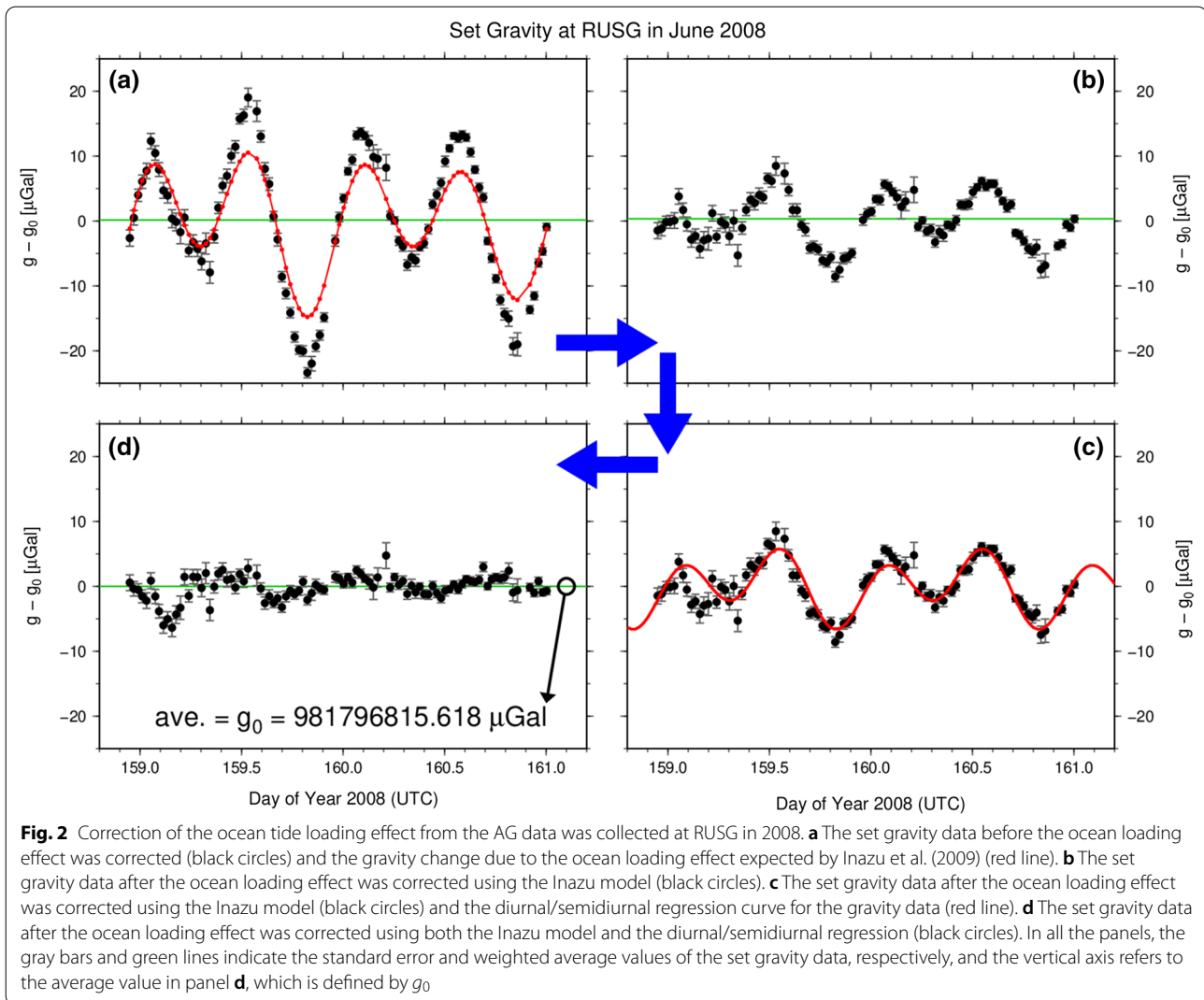
^a The gravity gradient value at the old AG point in 2006–2008 (Sun et al., 2010).

^b The gravity gradient value at the new AG point in 2012–2015. During the AG campaign measurement at MGVC in 2012, we observed the gravity difference between 0.0 and 100.0 cm heights from the new AG point using the LaCoste & Romberg's G578 relative gravimeter by ten times repeatedly, and determined the gravity gradient value by averaging the observed gravity difference values.

^c The 3-D distances from each AG point to the nearest glacier using the PDIM model (UAF07, Larsen et al. 2007).

^d Because the GNSS station of GUS2 was replaced to GUS6 on 20 June 2008, we named a hypothetical GNSS station GUS0 and created its continuous time series from those collected at GUS2 and GUS6 by removing coordinate steps due to the relocation of the GNSS station.

^e Nevada Geodetic Laboratory (NGL).



data to estimate the average gravity value at each AG point for each year (Fig. 2).

Moreover, we reprocessed past AG data collected from 2006 to 2008 (Sun et al. 2010; Sato et al. 2012) using the same procedures as above, and obtained a new data set of the AG at six gravity points in SE-AK from 2006 to 2015 (Table 2). The AG values are observed to decrease at all gravity points, mainly due to the past/present ice melting, which will be modeled and discussed later in the article. However, at the AG point located in Russell Island (RUSG), the AG in 2012 largely deviated from the decreasing trend, because the AG data still contained the effect of ground vibration due to the failure of a long-period spring (the so-called Superspring) in the FG5-111 gravimeter.

Absolute gravity rate of change

Effect of hydrological gravity disturbances

Since temporal AG variations can be caused by variation in the hydrological storage, its effect should be corrected from the observed AG data to quantify AG variation associated with GIA and PDIM. Although the effect is expected to be reduced due to the AG data being measured every June in the case of SE-AK (see the previous section), multi-year variations in land-water storage may be detected by the AG measurements. The SNOw TELelemetry (SNOTEL) data at Long Lake (green triangle in Fig. 1) showed less snow accumulation in 2006 and 2015, compared with those in the other years when the AG data were collected (Fig. 3a). This implies that the observed AG should decrease in 2006 and 2015, because less snow mass leads to smaller attraction force and greater unloading uplift.

Table 2 Reprocessed AG at gravity points in SE-AK

AG point	Year	Dates	AG value [μGal]	SD [μGal]	SE [μGal]	UC [μGal]	N_s	N_d
EGAN	2006	Jun14–Jun16	981760220.08	1.56	0.17	2.18	89	8834
	2007	May31–Jun02	981760219.75	1.10	0.14	2.12	66	6568
	2008	May30–Jun01	981760211.63	1.24	0.13	2.12	95	9437
	2012	Jun13–Jun15	981760207.25	1.70	0.13	2.12	169	16760
	2013	Jun10–Jun12	981760193.50	2.03	0.19	2.18	118	14082
	2015	May30–Jun02	981760194.66	2.52	0.22	2.13	133	13110
MGVC ^a	2006	Jun16–Jun18	981745281.62	1.73	0.16	2.10	119	11798
	2007	Jun02–Jun04	981745277.38	1.18	0.15	2.13	58	5718
	2008	Jun02–Jun04	981745272.62	1.22	0.12	2.15	96	9422
	2012	May31–Jun02	981745272.53	1.44	0.19	2.23	56	5473
	2013	Jun12–Jun15	981745259.39	2.53	0.25	2.13	104	12228
	2015	Jun14–Jun17	981745268.77	1.93	0.18	2.13	112	11051
GBCL	2006	Jun03–Jun05	981768410.16	1.48	0.15	2.08	92	9135
	2007	Jun04–Jun08	981768409.84	1.69	0.13	2.14	160	15952
	2008	Jun11–Jun13	981768398.93	1.81	0.17	2.13	116	11533
	2012	Jun04–Jun06	981768391.04	2.16	0.22	2.29	100	9846
	2013	Jun03–Jun04	981768384.24	3.00	0.32	2.17	90	8932
	2015	Jun05–Jun07	981768371.42	2.04	0.18	2.19	126	12527
RUSG ^b	2006	Jun07–Jun09	981796822.55	2.16	0.23	2.13	89	8708
	2007	Jun10–Jun12	981796822.41	1.35	0.14	2.17	92	9134
	2008	Jun07–Jun10	981796815.62	1.49	0.15	2.14	94	9334
	2012	Jun09–Jun10	981796832.52	25.43	2.86	3.81	79	7752
	2013	Jun07–Jun08	981796791.54	4.00	0.40	2.58	100	9638
	2015	Jun09–Jun11	981796783.91	2.25	0.23	2.12	100	9894
HNSG	2006	Jun11–Jun13	981832008.48	1.58	0.14	2.16	123	12205
	2007	Jun14–Jun17	981832003.60	1.70	0.15	2.14	128	12698
	2008	Jun15–Jun18	981831997.90	1.71	0.15	2.10	124	12288
	2012	Jun17–Jun18	981831990.15	1.64	0.17	2.15	92	9126
	2013	Jun16–Jun18	981831977.17	2.54	0.29	2.17	75	8863
	2015	Jun17–Jun19	981831973.66	1.60	0.16	2.12	101	9992
BRMC ^c	2007	Jun18–Jun20	981660211.75	1.47	0.15	2.15	94	9308
	2008	Jun19–Jun21	981660206.72	1.30	0.16	2.08	64	6297
	2012	Jun19–Jun21	981660201.73	1.50	0.16	2.14	90	8771
	2013	Jun19–Jun20	981660196.67	4.19	0.42	2.14	99	9776
	2015	Jun20–Jun22	981660186.23	2.08	0.20	2.07	113	10958

SD, SE, UC, N_s and N_d indicate the standard deviation, standard error, uncertainty, set and drop numbers, respectively. SE was calculated as the ratio of SD to the root of N_s . UC was estimated in the g9 software, by considering errors associated with instrumental systems and gravity data corrections.

^a The AG values at MGVC in 2012–2015 include the gravity difference between the old and new gravity points.

^b The AG at RUSG in 2012 has large errors due to the failure of the long-period spring in the FG5 gravimeter.

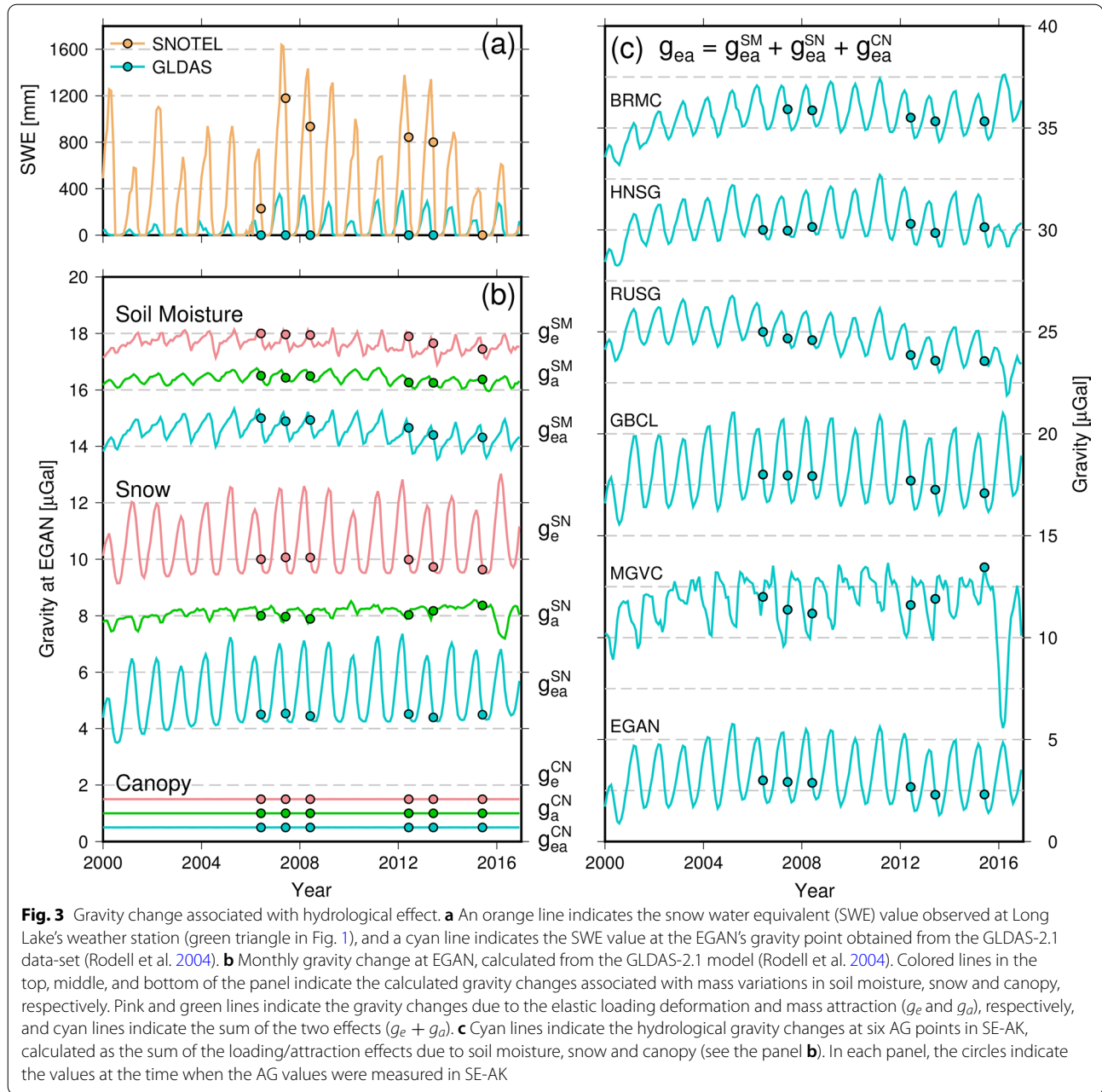
^c No AG measurement was conducted at BRMC in 2006.

Thus, we estimated gravity variations due to hydrological loading (Farrell 1972) and mass attraction (g_e and g_a , respectively) at each gravity point:

$$g_e(\phi_p, \lambda_p, t) = \rho_w \int H_w(\phi, \lambda, t) G_{ge}(\psi) dS \quad (1)$$

$$g_a(\phi_p, \lambda_p, t) = \rho_w \int H_w(\phi, \lambda, t) G_a(\phi, \lambda; \phi_p, \lambda_p) dS, \quad (2)$$

where (ϕ_p, λ_p) and (ϕ, λ) indicate the coordinates (latitude and longitude) of the gravity point and a loading point, respectively. ρ_w , $H_w(\phi, \lambda, t)$, $G_{ge}(\psi)$, $\psi = \psi(\phi, \lambda; \phi_p, \lambda_p)$,



and $G_a(\phi, \lambda; \phi_p, \lambda_p)$ also indicate the water density, the spatiotemporal distributions in water thickness, the elastic Green's function for gravity change due to point loading, the angular distance between (ϕ_p, λ_p) and (ϕ, λ) , and the Green's function for gravity change due to mass attraction, respectively. $G_{ge}(\psi)$ was prepared by linearly interpolating the original Green's function of the 1066A Earth model (Gilbert and Dziewonski 1975; Matsumoto et al. 2001) to obtain the loading response for each angular distance. $G_a(\phi, \lambda; \phi_p, \lambda_p)$ was also prepared by considering the Earth's curvature and topography:

$$G_a(\phi, \lambda; \phi_p, \lambda_p) = \frac{G}{r^2} \cdot \frac{r^2 + h_p^2 - \{h(\phi, \lambda)\}^2}{2rh_p}, \quad (3)$$

where G , $r = r(\phi, \lambda, h; \phi_p, \lambda_p, h_p)$, $h(\phi, \lambda)$, and h_p indicate the gravitational constant, the direct distance between the gravity and loading points, and the geocentric distances of the gravity and loading points, respectively. Here, we assumed that each hydrological mass was located on the corresponding cell of the ground, as expressed by the ETOPO1 digital elevation model (Amante and Eakins 2009). These Green's functions were then multiplied by

$\rho_w H(\phi, \lambda, t)$, i.e., the water density value multiplied by the spatiotemporal distributions of soil moisture, snow water equivalent and canopy in the Global Land Data Assimilation System version 2.1 (GLDAS-2.1) data set (Rodell et al. 2004). The gravity responses were finally estimated by spatially integrating the product of the Green's functions and water distribution (Eq. 1–2); cell sizes of the water distributions were defined as 0.0025^2 , 0.025^2 , and 0.25^2 deg² for $0.004 \leq \psi < 1.0$, $1.0 \leq \psi < 2.0$, and $2.0 \leq \psi$ deg, respectively, and the water distributions in $\psi < 0.004$ were excluded from the integral calculations to avoid singularity at $\psi \sim 0$ deg.

Figure 3b shows the estimated gravity variations due to soil moisture, snow, and canopy (abbreviated as SM, SN, and CN, respectively) at the EGAN gravity point (Fig. 1). Red, green, and blue lines indicate the loading effect (g_e^{XX}), the attraction effect (g_a^{XX}), and the sum of the two effects ($g_{ea}^{XX} = g_e^{XX} + g_a^{XX}$), respectively, for each hydrological component of XX ($= SM, SN$ or CN). g_e^{SM} , g_a^{SM} and g_e^{SN} change annually, reaching maxima in winter, mainly because of significant snow mass accumulation around SE-AK in winter (Fig. 3a). In contrast, g_a^{SN} reaches a minimum in winter, because accumulated snow in high mountains causes an upward attraction force (i.e., gravity decrease) to a gravity point located at the foot of the mountains. However, the amplitude of g_a^{SN} is smaller than that of g_e^{SN} , unless the gravity point is located close to mountains. Therefore, in the case of the EGAN's gravity point, g_{ea}^{SN} ($= g_e^{SN} + g_a^{SN}$) reaches a maximum in winter as well as g_e^{SN} .

The blue lines in Fig. 3c show the sum of g_{ea} for the three hydrological components ($= g_{ea}^{SM} + g_{ea}^{SN} + g_{ea}^{CN}$) at six gravity points (Fig. 1). g_{ea} at most of the gravity points reach a maximum in winter mainly due to snow loading (g_e^{SN} in Fig. 3b), although the gravity value is minimum in winter at MGVC due to the strong upward attraction force caused by snow mass accumulated on alpine glaciers near MGVC. Blue circles in Fig. 3c also indicate the hydrological gravity changes expected during the periods when the AG values were measured in SE-AK; their variation range is estimated to be approximately 2.5 μ Gal at MGVC and less than 1 μ Gal at the other gravity points.

Effect of coseismic gravity changes

Coseismic gravity changes should also be subtracted from the observed AG data to quantify the AG variation associated with GIA and PDIM. During the observation period from 2006 to 2015, two large earthquakes occurred near SE-AK as follows: [1] The Mw 7.8 Haida Gwaii earthquake occurred on 28 October 2012 because of slip on a low-angle thrust fault off the west coast of Moresby Island, Haida Gwaii (Nykolaishen et al. 2015).

Its epicenter was located approximately 640 km from the EGAN AG point (Fig. 4a). [2] The Mw 7.5 Craig Earthquake occurred on 5 January 2013 because of the strike slip along the Queen Charlotte Fault off the coast of SE-AK (Lay et al. 2013). Its epicenter was located approximately 290 km from the EGAN AG point (Fig. 4b).

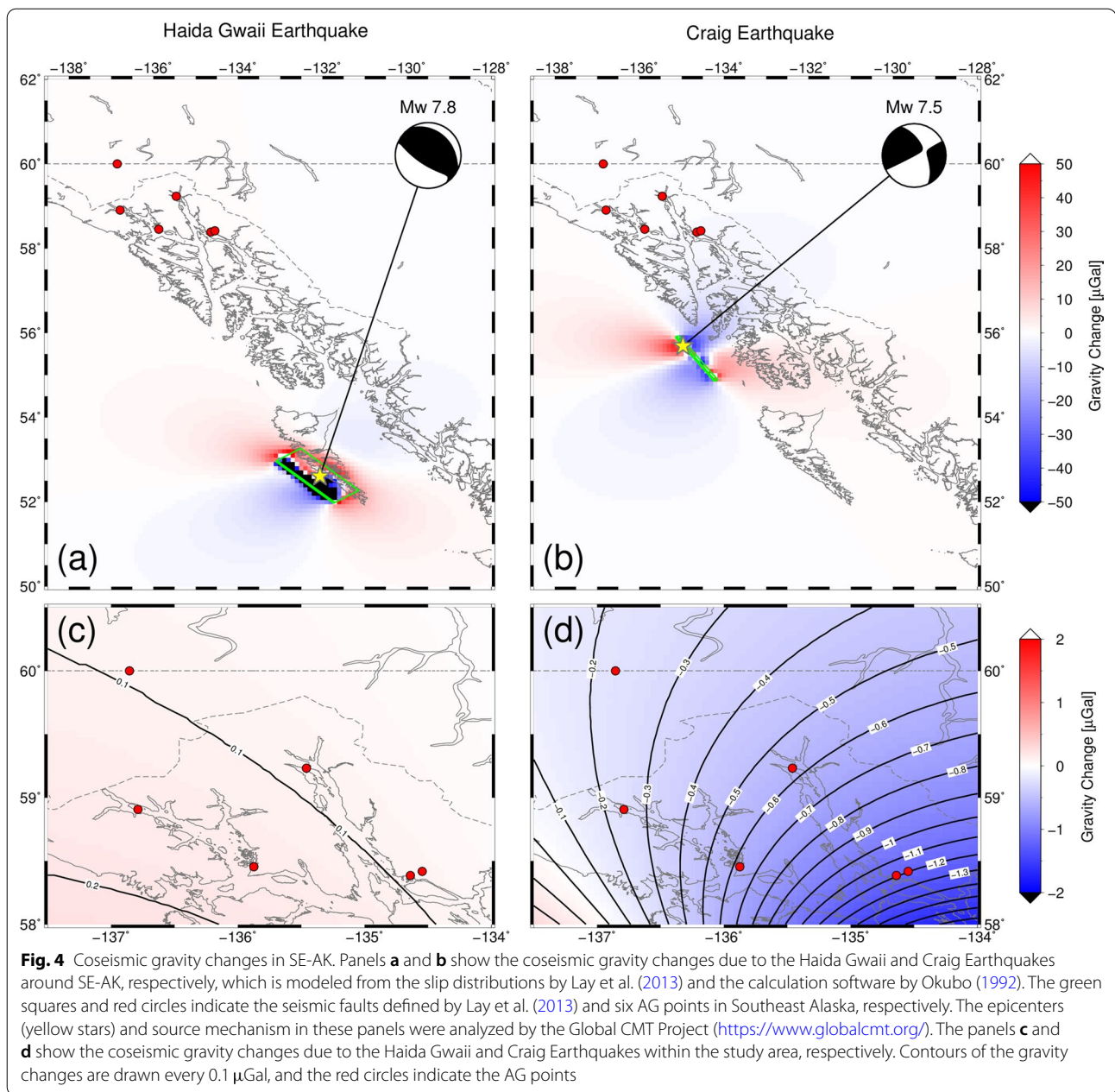
Figure 4c, d shows the coseismic gravity changes due to these two earthquakes, calculated on the basis of the dislocation theory of Okubo (1992) and slip distribution models by Lay et al. (2013). A small gravity increase of up to 0.15 μ Gal was expected at the AG points during the 2012 Haida Gwaii earthquake (Fig. 4c) mainly because of the small ground subsidence at the AG points caused by the coseismic slip. In contrast, a significant gravity decrease of up to 1.2 μ Gal was expected during the 2013 Craig Earthquake (Fig. 4d), because the coseismic slip in the vicinity of SE-AK led to a ground uplift of up to 4 mm at the AG points.

We disregarded temporal gravity changes due to post-seismic deformations. In fact, post-seismic vertical displacement of up to 6 mm was observed near the epicenter of the Haida Gwaii earthquake (Nykolaishen et al. 2015), although no significant post-seismic displacement was detected around our AG points in the SE-AK area, according to the GNSS time series obtained by Nevada Geodetic Laboratory (Blewitt et al. 2018).

Updated gravity variation rate

Red circles in Fig. 5 indicate the AG at the six gravity points after the effects of hydrology and the two earthquakes were corrected from the original AG data (green circles). The corrections are typically less than 1 μ Gal, but it is as large as 1.80 μ Gal at EGAN in 2013 mainly because of the coseismic gravity decrease owing to the 2013 Craig earthquake (Fig. 4d).

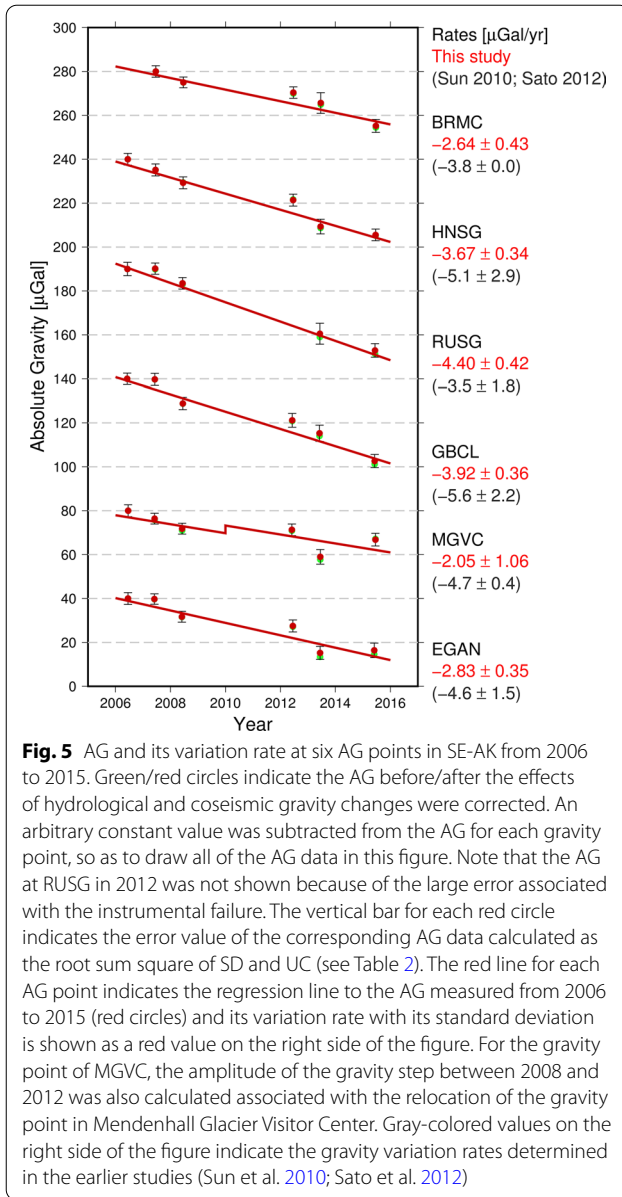
We calculated a new gravity variation rate at each gravity point from the corrected AG from 2006 to 2015 (red circles in Fig. 5) using the weighted least-square adjustment. We here defined the weight of each AG campaign by the inverse square of the error value, which was calculated by the root sum square of the standard deviation and uncertainty values (SD and UC, respectively; see Table 2). In addition, we calculated a gravity step at MGVC between 2008 and 2012 in the least-squares calculation, because we had to relocate the AG point by about 5 m in June 2012 due to an exhibit installed on the old AG point by the visitor center (see Appendix A). We also excluded the AG obtained at RUSG in 2012, because it contained a large error associated with the failure of the FG5-111 gravimeter (see the section of "Absolute gravity data").



The red lines in Fig. 5 indicate the updated AG variation rates at the six gravity points. Our variation rates were estimated with smaller errors (see the right side of Fig. 5) than those obtained in earlier studies (Sun et al. 2010; Sato et al. 2012) at most gravity points, because new AG data from 2012 to 2015 were added to estimate the AG variation rate. However, the error of the variation rate at MGVC ($\pm 1.06 \mu\text{Gal/yr}$) was about twice as great as that obtained by Sun et al. (2010), because the AG values from 2012 to 2015 deviated from the linear gravity trend. The deviation of the AG data also caused the poor

estimate of the gravity step associated with the relocation of the MGVC gravity point ($+3.53 \pm 7.01 \mu\text{Gal}$).

At most of the AG points, the updated gravity variation rates are smaller by up to $2.8 \mu\text{Gal/yr}$ than those reported by the earlier studies (Sun et al. 2010; Sato et al. 2012). The gravity variation rate is greatest (in absolute) at RUSG in all of the AG points; this result is consistent with the spatial pattern of uplift associated with the GIA and PDIM (Fig. 1). The difference of the gravity variation rates between EGAN and MGVC reaches approximately $0.8 \mu\text{Gal/yr}$ despite the close distance (approximately 6.6



km; see Fig. 1), because the glacier mass loss on the top of the mountain glaciers can decrease the upward attraction force (i.e., increase the gravity value) at MGVC, as demonstrated in the next section.

Numerical calculation of gravity variation rate

The observed gravity variation rates (Fig. 5) were then compared with those calculated using the GIA/PDIM models. We basically follow the calculation procedures of Sato et al. (2011, 2012), because we will also compare our calculation results with their results later. In the case of SE-AK, the GIA source can be separated into four components: global past ice melting (GPIM), regional past ice

melting (RPIM), local past ice melting (LPIM) and present-day ice melting (PDIM). We numerically calculated the gravity variation rates due to four GIA components, along with the time variation in attraction force due to PDIM.

The effect of global past ice melting (GPIM)

Rate of temporal gravity variation due to past ice melting (denoted by \dot{g}_v) can be calculated using the load deformation theory for the viscoelastic medium (Peltier 1974):

$$\dot{g}_v(\phi_p, \lambda_p, t_0) = \rho_i \iint \Delta H_i(\phi, \lambda, s) \dot{G}_{gv}(\psi, t_0 - s) dS ds, \quad (4)$$

where t_0 , ρ_i , and $\Delta H_i(\phi, \lambda, s)$ indicate the present time, the typical glacier density ($= 850 \text{ kg/m}^3$; Huss 2013; Hu and Freymueller 2019), and the spatiotemporal distribution in glacier melting at a time s , respectively. $\dot{G}_{gv}(\psi, t_0 - s)$ also indicate the time derivative of the viscoelastic Green's function for gravity variation at a time t_0 caused by the point loading on the Maxwell Earth at a time s :

$$\begin{aligned} \dot{G}_{gv}(\psi, t_0 - s) &= \frac{g_0}{m_e} \sum_{n=0}^{n_{max}} \dot{\delta}_n(t_0 - s) P_n(\cos \psi) \\ &= \frac{g_0}{m_e} \sum_{n=0}^{n_{max}} \{-2\dot{h}_n(t_0 - s) + (n+1) \\ &\quad \dot{k}_n(t_0 - s)\} P_n(\cos \psi) \end{aligned} \quad (5)$$

where g_0 and m_e indicate the typical absolute gravity values ($= 9.8065 \text{ m/s}^2$) and Earth's mass ($= 5.97 \times 10^{24} \text{ kg}$), respectively. \dot{h}_n , \dot{k}_n and P_n also indicate the time derivatives of load Love numbers and the Legendre polynomial for the n -th degree, respectively. δ_n and \dot{h}_n are proportional to the rates of gravity variation and vertical deformation due to a unit load, respectively (see Eqs. 15, 16). The load Love numbers (\dot{h}_n and \dot{k}_n) were calculated using the ALMA software (Spada 2008), with the assumption of a spherically symmetric, incompressible, and Maxwell viscoelastic Earth. The summation of Eq. (5) was performed up to the degree of $n_{max} = 180$, because the loading response to past ice melting converges to its asymptotic value at a degree of $n \sim 130$ (e.g., Fig. 4 in Sato et al. 2011).

We estimated the present-day gravity variation due to the GPIM for each gravity point p (denoted by $\dot{g}_v^{GPIM}(\phi_p, \lambda_p, t_0)$), using the global historical deglaciation model ICE-6G_C (Peltier et al. 2015) for ΔH_i in Eq. (4). We also calculated the load Love numbers (\dot{h}_n and \dot{k}_n in Eq. 5) by applying the viscosity value in the VM5a model (Peltier et al. 2015), and the values of density and shear modulus in the Preliminary Reference Earth Model

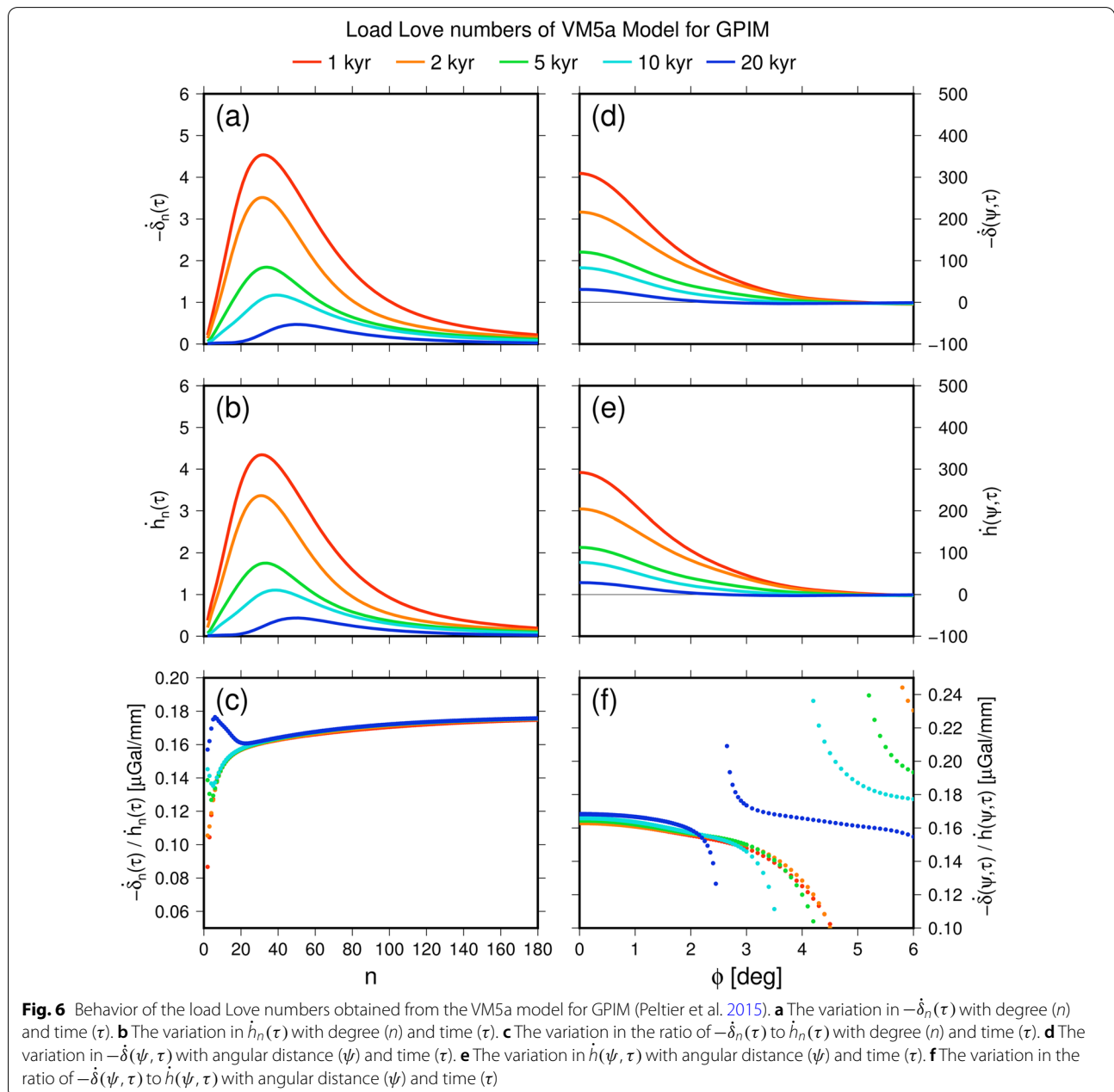
(PREM) model (Dziewonski and Anderson 1981) using the ALMA software (Spada 2008). The load Love numbers and the resulting Green's function (\dot{G}_{gv} in Eqs. 4–5) were calculated at the time step of 0.5 kyr, which is consistent with that for the ICE-6G_C deglaciation model.

Figure 6a–c indicates the behavior of $-\dot{\delta}_n(\tau)$ and $\dot{h}_n(\tau)$ to the spherical harmonic degree (n) for the VM5a model, where $\tau = t_0 - s$ (see Eqs. 4–5). Both $-\dot{\delta}_n(\tau)$ and $\dot{h}_n(\tau)$ reach their maxima at $n = 30$ –50, and the ratio of $-\dot{\delta}_n(\tau)/\dot{h}_n(\tau)$ is constant in time, despite the temporal

decrease in $-\dot{\delta}_n(\tau)$ and $\dot{h}_n(\tau)$. Figure 6d–f also indicates the variations of $-\dot{\delta}(\psi, \tau)$ and $\dot{h}(\psi, \tau)$ to the angular distance from a loading point, ψ :

$$\dot{\delta}(\psi, \tau) = \sum_{n=0}^{n_{max}} \dot{\delta}_n(\tau) P_n(\cos \psi), \quad (6)$$

$$\dot{h}(\psi, \tau) = \sum_{n=0}^{n_{max}} \dot{h}_n(\tau) P_n(\cos \psi). \quad (7)$$



$-\dot{\delta}(\psi, \tau)$ and $\dot{h}(\psi, \tau)$ reaches its maximum at $\psi = 0$ deg, and they decrease with the increments of ψ and τ . The ratio of $-\dot{\delta}(\psi, \tau)/\dot{h}(\psi, \tau)$ also depends on the time, mainly because the position of ψ , where $\dot{h}(\psi, \tau) = 0$ varies with time. However, $-\dot{\delta}(0, \tau)/\dot{h}(0, \tau)$ is nearly constant (0.16–0.17 $\mu\text{Gal}/\text{mm}$) at any time, and its constant value is close to the Bouguer approximation value (e.g., Ekman and Mäkinen 1996; James and Ivins 1998). All of these characteristics about the load Love numbers agree well with past studies (e.g., Figs. 1–2 in Olsson et al. 2015).

The effects of regional/local past ice melting (RPIM and LPIM)

To accurately calculate gravity variations caused by rapid ice melting since the end of the LIA in SE-AK, we additionally utilize the spatiotemporally high-resolution ice melting models denoted by RPIM and LPIM. The RPIM model is identical to the regional model in Larsen et al. (2004, 2005), and is composed of 531 disk loads with a 20 km diameter in South and Southeast Alaska (see Fig. 2.4 in Larsen 2003). This model was developed by extrapolating the ice melting rate of Arendt et al. (2002) to the end of the LIA in 1900. The LPIM model is also identical to the Glacier Bay model in Larsen et al. (2004, 2005), and was constructed based on aerophotography and field investigations. This model consists of five disk loads with 26–39 km diameters on the Glacier Bay area (see Fig. 5a in Larsen et al. 2005).

As the effects of RPIM and LPIM are sensitive to the viscoelastic structure beneath SE-AK, we determine optimum parameters for the structure via the following grid search calculation. We first assume that the asthenosphere is composed of four viscoelastic layers (Table 3), and use the structure model of Sato et al. (2011, 2012) for most of the parameters except for the lithospheric thickness (d) and upper mantle viscosity (η). Note that the elastic parameters (density, shear, and bulk moduli) were

defined in Sato et al. (2011, 2012) by averaging the parameter values of the PREM model (Dziewonski and Anderson 1981). We also choose a pair of (d, η) in the range of $30 \leq d \leq 120$ [km] and $0.5 \times 10^{19} \leq \eta \leq 5.0 \times 10^{19}$ [Pa s], and calculate the load Love numbers and the consequent Green's function (Eq. 5) using the ALMA software (Spada 2008). The gravity variation rates due to RPIM and LPIM for each gravity point (p) are then estimated according to Eq. (4), and are denoted by $\dot{g}_v^{RPIM}(\phi_p, \lambda_p, t_0; d, \eta)$ and $\dot{g}_v^{LPIM}(\phi_p, \lambda_p, t_0; d, \eta)$, respectively. During the numerical integral of Eq. (4), the disk loads of the RPIM and LPIM models were converted to point loads with a cell size of 0.01 degree. These calculations are repeated for all pairs of (d, η) with grid intervals of $\Delta d = 10$ km and $\Delta \eta = 0.5 \times 10^{19}$ Pa s, and the optimum pair of (d, η) is finally determined to minimize the χ^2 value:

$$\chi^2(d, \eta) = \sum_p \left[\frac{\dot{g}_{obs}(\phi_p, \lambda_p) - \dot{g}_{cal}(\phi_p, \lambda_p, t_0; d, \eta)}{\sigma_{obs}(\phi_p, \lambda_p)} \right]^2, \quad (8)$$

$$\begin{aligned} \dot{g}_{cal}(\phi_p, \lambda_p, t_0; d, \eta) &= \dot{g}_v(\phi_p, \lambda_p, t_0; d, \eta) + \dot{g}_{ea}(\phi_p, \lambda_p) \\ &= \left[\dot{g}_v^{GPIM}(\phi_p, \lambda_p, t_0) \right. \\ &\quad + \dot{g}_v^{RPIM}(\phi_p, \lambda_p, t_0; d, \eta) \\ &\quad + \dot{g}_v^{LPIM}(\phi_p, \lambda_p, t_0; d, \eta) \left. \right] \\ &\quad + \dot{g}_{ea}^{PDIM}(\phi_p, \lambda_p). \end{aligned} \quad (9)$$

In Eq. (8), $\dot{g}_{obs}(\phi_p, \lambda_p)$ and $\sigma_{obs}(\phi_p, \lambda_p)$ indicate the observed gravity variation rate and its error value for each gravity point p , respectively. In Eq. (9), $\dot{g}_{ea}^{PDIM}(\phi_p, \lambda_p)$ indicates the gravity variation rate due to PDIM, as described in the next section.

Note that we calculate the GIA responses using different rheological structures for GPIM and RPIM/LPIM, but this article does not claim the possibility of the time variation in the rheological structure under SE-AK. As described in the previous section, the GPIM model (i.e., the ICE-6G_C's ice-melting history and the VM5a's rheological structure; Peltier et al. 2015) is used for calculating the GIA effect due to long-term global ice melting especially just after the Last Glacial Maximum, but the ICE-6G_C's spatiotemporal resolution is too low (1 deg and 500 yr) to estimate GIA response associated with spatiotemporally smaller ice-melting events. In addition, ICE-6G and VM5a should not be used separately, because Peltier et al. (2015) reproduced the global GIA response with the combination of ICE-6G and VM5a. Therefore, we here define another rheological structure for RPIM and LPIM, as previous studies have done (Sato et al. 2011, 2012; Hu and Freymueller 2019), in order to

Table 3 Rheological structure defined for RPIM and LPIM

Layer	Radius [km]		Thickness [km]	Viscosity [10^{19} Pa s]
	Bottom	Top		
Lithosphere	6371 – d	6371	d (= 30 to 120)	Infinity
Asthenosphere 1	6151	6371 – d	220 – d	η (= 0.5 to 5.0)
Asthenosphere 2	5971	6151	180	40.0
Asthenosphere 3	5701	5971	270	40.0
Asthenosphere 4	3480	5701	2221	200.0
Liquid core	0	3480	3480	0.0

reproduce the GIA-derived gravity change mainly due to the significant ice melting in/around SE-AK after LIA.

The effects of present-day ice melting (PDIM)

Gravity variation associated with PDIM can be divided into loading and attraction effects. We calculated the gravity variation rates due to two effects (\dot{g}_e and \dot{g}_a , respectively) by referring to Eqs. (1) and (2):

$$\dot{g}_e(\phi_p, \lambda_p) = \rho_i \iint \dot{H}_i(\phi, \lambda) G_{ge}(\psi) dS, \quad (10)$$

$$\dot{g}_a(\phi_p, \lambda_p) = \rho_i \iint \dot{H}_i(\phi, \lambda) G_a(\phi, \lambda; \phi_p, \lambda_p) dS, \quad (11)$$

where $\dot{H}_i(\phi, \lambda)$ indicates the spatial distribution of PDIM's rate. In this calculation, we used the same Green's functions ($G_{ge}(\psi)$ and $G_a(\phi, \lambda; \phi_p, \lambda_p)$) as for calculating the hydrological gravity variations (see the section titled "Effect of hydrological gravity disturbances").

We utilized the PDIM models of UAF05 (Arendt et al. 2002; Larsen et al. 2005) and UAF07 (Larsen et al. 2007) for $\dot{H}_i(\phi, \lambda)$. UAF05 provides the spatial distribution of ice elevation change from the mid-1950s to the mid-1990s, and covers South/Southeast Alaska (-150° to -130° E and $+55.5^\circ$ to $+62.5^\circ$ N) with grid intervals of approximately 0.01° and 0.005° for longitude and latitude, respectively. UAF07 also provides the ice thickness change in SE-AK (-139.5° to -132.0° E and $+56.5^\circ$ to $+60.0^\circ$ N) from 1948 to 2000, and its grid interval is 0.000556° for both longitude and latitude. We merged two PDIM models to calculate the PDIM-derived gravity variations (Eqs. 10–11). In the merged PDIM model, UAF07 was used for SE-AK, and UAF05 was additionally used for the rest of South/Southeast Alaska. Therefore, the sum of the PDIM effect can be written as follows:

$$\begin{aligned} \dot{g}_{ea}^{PDIM}(\phi_p, \lambda_p) &= \dot{g}_e^{PDIM}(\phi_p, \lambda_p) + \dot{g}_a^{PDIM}(\phi_p, \lambda_p) \\ &= \dot{g}_e^{UAF07}(\phi_p, \lambda_p) + \dot{g}_e^{UAF05}(\phi_p, \lambda_p) \\ &\quad + \dot{g}_a^{UAF07}(\phi_p, \lambda_p) + \dot{g}_a^{UAF05}(\phi_p, \lambda_p). \end{aligned} \quad (12)$$

Note that we here use the elastic Green's function ($G_{ge}(\psi)$) based on the 1066A's Earth model (Gilbert and Dziewonski 1975; Matsumoto et al. 2001), although the elastic structure of the PREM's Earth model (Dziewonski and Anderson 1981) is also utilized for calculating the effects of GPIM, RPIM and LPIM. According to our preliminary calculation, \dot{g}_e^{PDIM} can differ by up to $0.13 \mu\text{Gal}/\text{yr}$ if we use $G_{ge}(\psi)$ based on PREM instead. This difference value is only 3.7 % of the observed gravity variation rate at a maximum, and it is also smaller than the error range of the observed rate (Fig. 5). In these respects, the

choice of the Earth model between 1066A and PREM for $G_{ge}(\psi)$ is not significant in discussing the rapid gravity change observed in SE-AK.

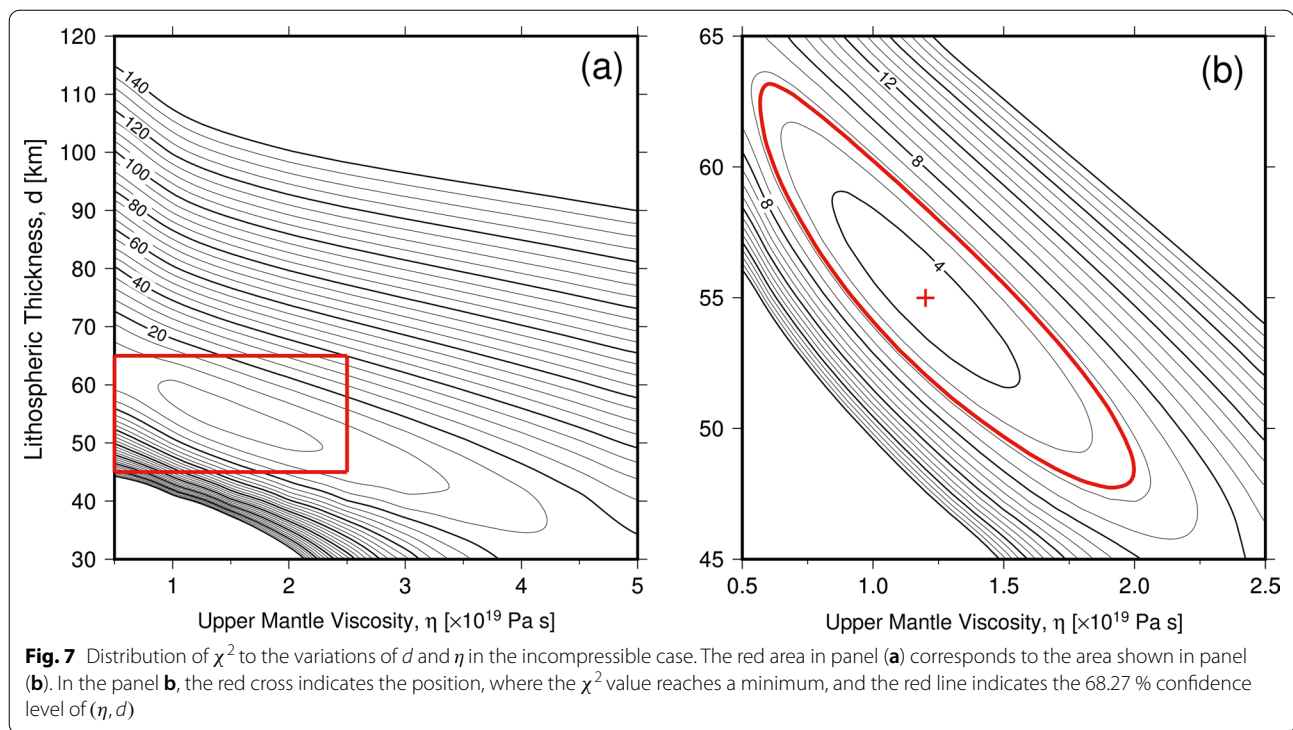
Results

Optimal rheological parameters

Figure 7a shows the distribution of χ^2 for the variations in d and η . χ^2 has a trade-off between d and η , i.e., for a certain value of χ^2 , d decreases as η increases. This trade-off can be explained by the positive correlation between asthenospheric viscosity (η) and the cube of the asthenospheric thickness (denoted by D^3) for a constant relaxation time value (e.g., Richards and Lenardic 2018). Because $d + D = 220$ km in our case (Table 3), the synthetic gravity time series and consequent χ^2 value remain constant as long as d is negatively correlated to η . The minimum χ^2 value is less than five, and the parameter ranges for $\chi^2 = 5$ are $50 \leq d \leq 60$ km and $1 \times 10^{19} \leq \eta \leq 2 \times 10^{19}$ Pa s. However, the grid widths are too coarse ($\Delta d = 10$ km and $\Delta \eta = 0.5 \times 10^{19}$ Pa s) to determine an optimum pair of (d, η) more precisely.

Figure 7b shows the distribution of χ^2 obtained from an additional grid search calculation with smaller grid widths ($\Delta d = 2$ km and $\Delta \eta = 0.1 \times 10^{19}$ Pa s). This calculation was applied to the range of $45 \leq d \leq 65$ km and $0.5 \times 10^{19} \leq \eta \leq 2.5 \times 10^{19}$ Pa s (red squares in Fig. 7a). χ^2 reaches a minimum value of $\chi_{min}^2 = 3.39$ at $d = 55$ km and $\eta = 1.2 \times 10^{19}$ Pa s (red cross in Fig. 7b). These optimal values of (d, η) are consistent with those determined in earlier studies using GNSS data (Sato et al. 2011; Hu and Freymueller 2019) under the common assumption of the incompressible Earth. In addition, the χ_{min}^2 value is close to the degree of freedom in the case of our grid search calculation ($= 6 - 2 = 4$), and this indicates that our calculation is statistically plausible.

Here, we define the error range of χ^2 as $\chi^2 \leq \chi_{min}^2 + \Delta \chi^2$, where $\Delta \chi^2$ indicates the 68.27 % confidence level in the chi-squared test. Since $\Delta \chi^2 = 2.30$ for two variables, the error range of χ^2 is calculated to be $3.39 + 2.30 = 5.69$ (red line in Fig. 7b), and the resultant error ranges for (d, η) are obtained as $47 \leq d \leq 64$ km and $0.5 \times 10^{19} \leq \eta \leq 2.0 \times 10^{19}$ Pa s. Our error ranges are smaller than those of Hu and Freymueller (2019) by about 32 and 50 % for d and η , respectively. Their error ranges may be enlarged, because one more parameter (i.e., asthenospheric thickness) was determined using their grid search analysis. These results indicate that absolute gravimetry, as well as GNSS observations (Sato et al. 2011; Hu and Freymueller 2019) can precisely determine rheological parameters for the uppermost layers of the Earth.



The behavior of load Love numbers for RPIM and LPIM

Figure 8 indicates the behavior of the Green's function obtained using the optimum rheological model for RPIM and LPIM (red cross in Fig. 7b). This figure is similar to Fig. 6, showing the load Love numbers of the VM5a model for GPIM, although the ranges of the vertical axes in panels (a), (b), (d), and (e) differ between the two figures. Both $-\delta_n(2 \text{ kyr})$ and $\dot{h}_n(2 \text{ kyr})$ reach maxima at $n = 38$ (blue lines in Fig. 8a, b), and their peak values are nearly the same as those obtained from the VM5a model (dashed gray lines in Fig. 8a, b). However, the peak values of $-\delta_n(1 \text{ kyr})$ and $\dot{h}_n(1 \text{ kyr})$ from our optimum model (the cyan lines in Fig. 8a, b) are approximately 2.8 times greater than those from the VM5a model (red lines in Fig. 6a, b). These results indicate that the structure of the Earth of our optimum model responds to the past ice unloading of $\tau < 2 \text{ kyr}$ more strongly than that of the VM5a model, and the same characteristics was observed in the panels of $-\delta(\psi, \tau)$ and $\dot{h}(\psi, \tau)$ (Fig. 8d, e, respectively). These characteristics are caused by the fact that the asthenospheric viscosity in our optimum model ($1.2 \times 10^{19} \text{ Pa s}$) is about 1/40 of that in the VM5a model ($5.0 \times 10^{20} \text{ Pa s}$), and consequently the relaxation time is much shorter in our model.

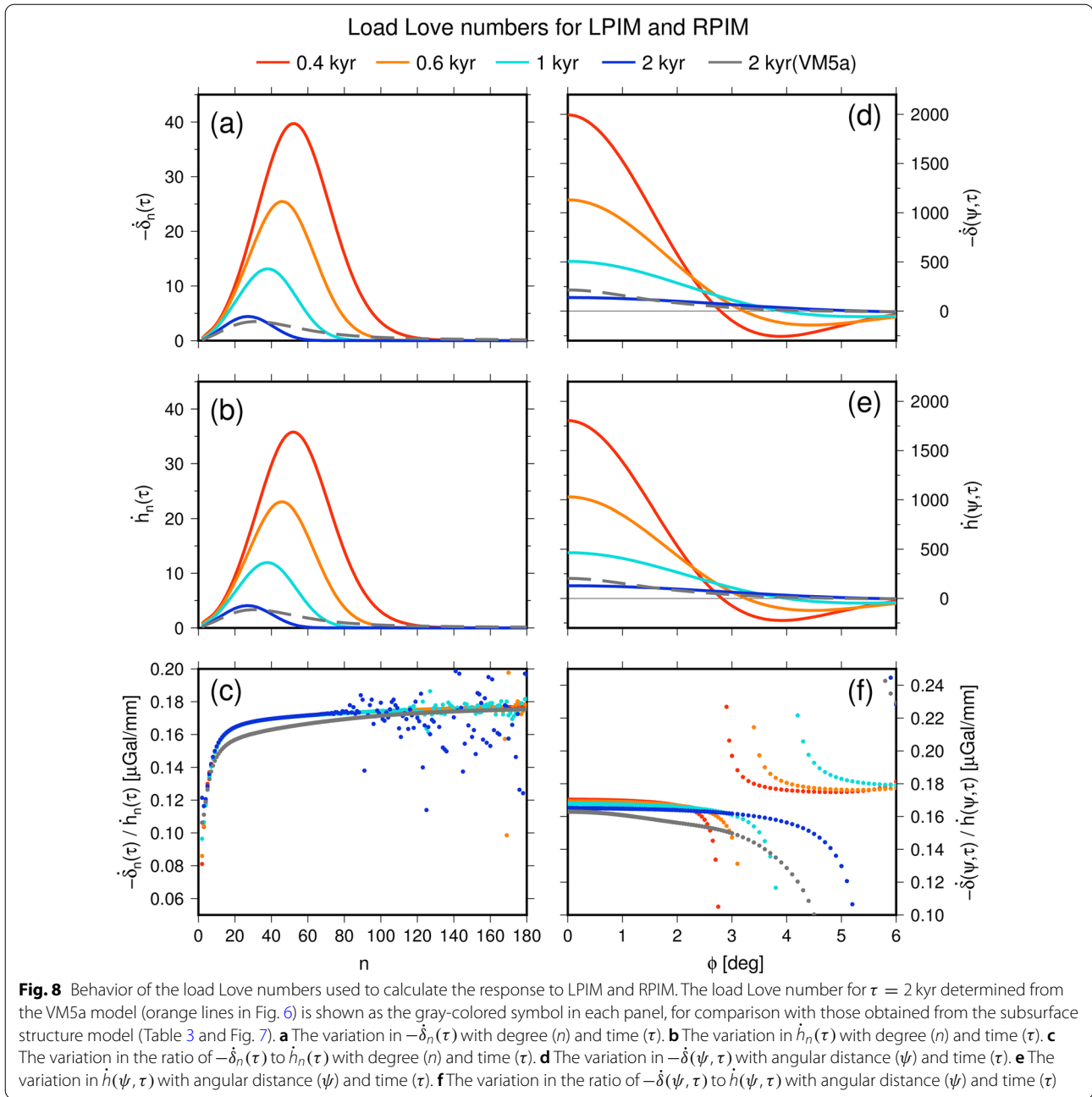
Contrarily, the ratio of $-\dot{\delta}/\dot{h}$ in our model is consistent with that in the VM5a model. For example, the asymptotic value of $-\dot{\delta}_n(\tau)/\dot{h}_n(\tau)$ at $n \rightarrow 180$ is 0.17–0.18 $\mu\text{Gal}/\text{mm}$ in both models (Figs. 6c and 8c), although the

ratio value diverges at $n > 80$ in our model because of the division by $\dot{h}_n(\tau) \simeq 0$. In addition, $-\dot{\delta}(0, \tau)/\dot{h}(0, \tau)$ is 0.16–0.17 $\mu\text{Gal}/\text{mm}$, which is common for any time and structure model (Figs. 6f and 8f). These results imply that the ratio of gravity change to vertical deformation tends to be independent of the structure of the Earth, as discussed in the earlier studies (e.g., Wahr et al. 1995; Fang and Hager 2001).

Calculated gravity variation rates

Figure 9 shows the calculated gravity variation rates due to the effects of GPIM, RPIM, LPIM, and PDIM (\dot{g}_v^{GPIM} , \dot{g}_v^{RPIM} , \dot{g}_v^{LPIM} and \dot{g}_{ed}^{PDIM} , respectively) at each gravity point. The mean of \dot{g}_v^{GPIM} (purple bars) is approximately $-0.37 \mu\text{Gal}/\text{yr}$, which is smaller than both \dot{g}_v^{RPIM} and \dot{g}_v^{LPIM} , and the difference in \dot{g}_v^{GPIM} between the gravity points was also small (within approximately 0.10 μGal). This is because the gravity points in SE-AK are located far from the Laurentide ice sheet, which had covered North America and Canada until about 14 kyr BP (Peltier et al. 2015).

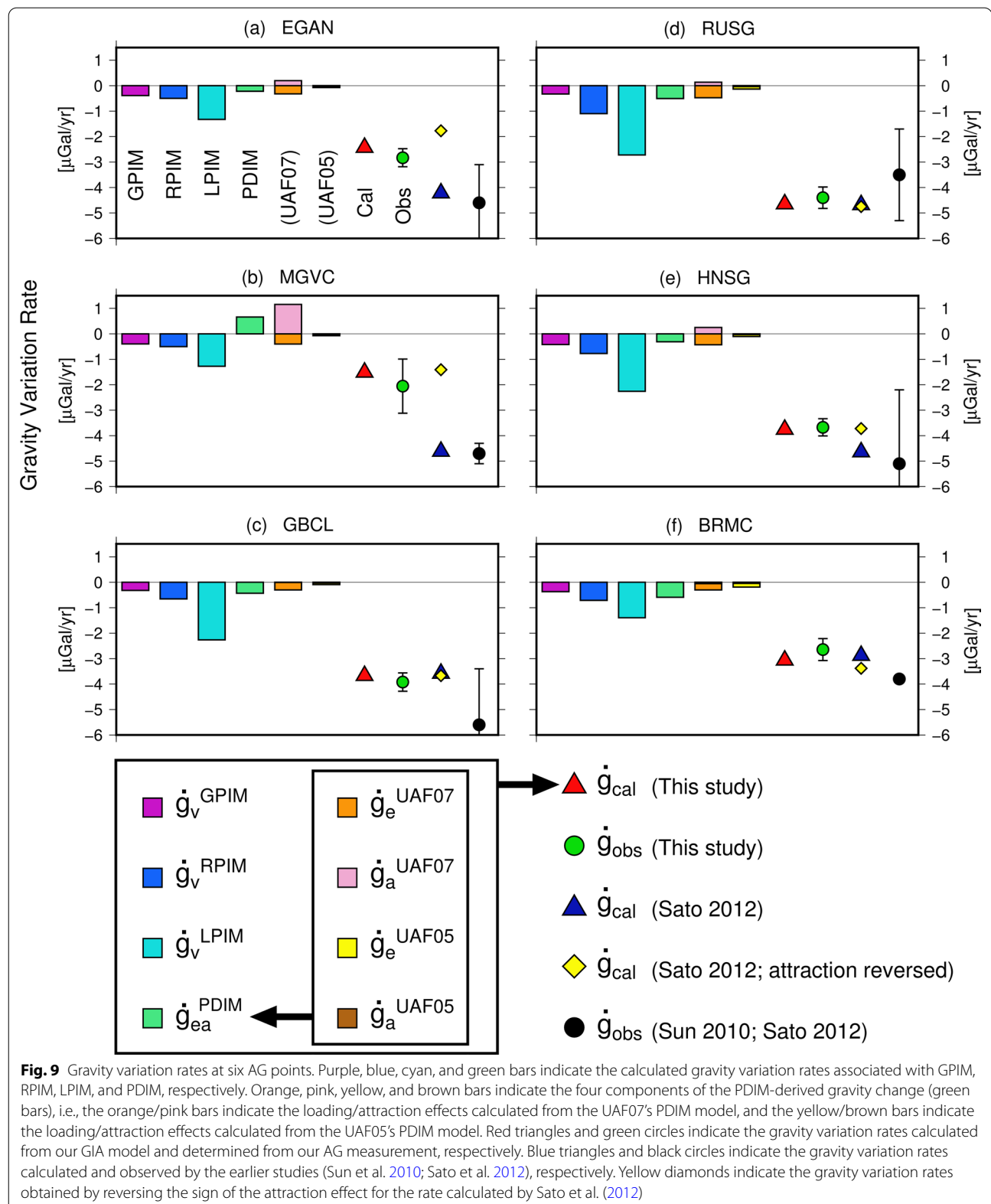
\dot{g}_v^{LPIM} and \dot{g}_v^{RPIM} (blue and cyan bars in Fig. 9) are the first and second largest ice melting effects at each gravity point and their averages (-1.87 and $-0.71 \mu\text{Gal}/\text{yr}$) are about 5 and 2 times greater than that of \dot{g}_v^{GPIM} , respectively. This is because a significant mass of glaciers has melted in SE-AK in the last 100 years. Particularly, \dot{g}_v^{LPIM} at GBCL, RUSG, and HNSG is about twice as large



as that at the other gravity points, because three gravity points are located in the center of the Glacier Bay area, where the significant ice mass has rapidly melted since LIA.

In the PDIM effects, the contribution of \dot{g}_e^{UAF07} (orange bars in Fig. 9) is the largest at almost all gravity points, because UAF07's PDIM model covers SE-AK, in which we measured the AG. \dot{g}_a^{UAF07} (pink bars) is positive at most gravity points, because the glacier melting at a higher position relative to a gravity point leads to the

weakening of the upward attraction force (i.e., the gravity increase). In particular, \dot{g}_a^{UAF07} at MGVC is about 10 times larger than its average at the other five gravity points, and the contribution of \dot{g}_a^{UAF07} is the greatest for all PDIM effects at MGVC only. In fact, the MGVC gravity point is located in the Mendenhall Glacier Visitor Center, and closest to glaciers of all the gravity points (Table 1). Green bars indicate the sum of the four PDIM effects (i.e., $\dot{g}_{ea}^{PDIM} = \dot{g}_e^{UAF07} + \dot{g}_a^{UAF07} + \dot{g}_e^{UAF05} + \dot{g}_a^{UAF05}$), whereas \dot{g}_{ea}^{PDIM} is positive (+0.66 $\mu\text{Gal}/\text{yr}$) at MGVC due to the



\dot{g}_a^{UAF07} 's contribution, and it is negative (-1 to 0 $\mu\text{Gal}/\text{yr}$) at the other AG points due to the contribution of \dot{g}_e^{UAF07} .

Red triangles in Fig. 9 show the sum of all effects calculated in this study ($\dot{g}_{cal} = \dot{g}_v^{GPIM} + \dot{g}_v^{RPIM} + \dot{g}_v^{LPIM} + \dot{g}_{ea}^{PDIM}$). \dot{g}_{cal} is larger (in absolute value) at gravity points close to Glacier Bay, such as RUSG, HNSG, and GBCL (-4.65 , -3.76 and -3.67 $\mu\text{Gal}/\text{yr}$, respectively), and this feature is consistent with GNSS observations (Fig. 1). On the other hand, the difference in \dot{g}_{cal} between EGAN and MGVC (-2.43 and -1.51 $\mu\text{Gal}/\text{yr}$, respectively) is as large as approximately 1 $\mu\text{Gal}/\text{yr}$, even though the two AG points are close together (approximately 6.5 km) and have almost the same uplift rate (Fig. 1). The difference in \dot{g}_{cal} is nearly equal to that in \dot{g}_a^{UAF07} between the two gravity points, which indicates that the attraction effect of PDIM is strongly affected at MGVC. \dot{g}_{cal} is consistent with \dot{g}_{obs} (green circles) within the error range of \dot{g}_{obs} at all gravity points, and the root-mean-square (RMS) difference was calculated to be approximately 0.36 $\mu\text{Gal}/\text{yr}$. According to the earlier studies, the RMS difference between \dot{g}_{obs} (black circles; Sun et al. 2010) and \dot{g}_{cal} (blue triangles; Sato et al. 2012) was approximately 1.06 $\mu\text{Gal}/\text{yr}$. Hence, the RMS value in our results is approximately 60% smaller than obtained by Sun et al. (2010) and Sato et al. (2012). In fact, Sato et al. (2012) calculated \dot{g}_{cal} using rheological parameters of Sato et al. (2011). They determined the parameters from the vertical deformation rate of the GNSS time series (e.g., Larsen et al. 2004), not from the gravity variation rates in Sun et al. (2010). In contrast, we determined the optimal rheological parameters (Fig. 7) so as to conform \dot{g}_{cal} with \dot{g}_{obs} (Fig. 5), and hence, we naturally obtained the resultant \dot{g}_{cal} values with the smaller RMS residual. We would like to emphasize here that we succeeded in determining the rheological parameters robustly due to the accurate gravity variation rates observed from the long-term repeated AG measurements in SE-AK.

Our \dot{g}_{cal} values (red triangles) were significantly different from those of Sato et al. (2012) (blue triangles) by approximately 1.5 $\mu\text{Gal}/\text{yr}$ in the RMS, even though our rheological parameters agreed well with those by Sato et al. (2011). The deviation of \dot{g}_{cal} may be caused by the incorrect sign of the attraction effect of the PDIM in the estimation of Sato et al. (2012) as follows: We can calculate the attraction effect due to PDIM according to Sato et al. (2012) as

$$\dot{g}_a^{Sato}(\phi_p, \lambda_p) = \dot{g}^{Sato}(\phi_p, \lambda_p) - \beta_B \cdot \dot{u}_e^{Sato}(\phi_p, \lambda_p), \quad (13)$$

where \dot{g}^{Sato} indicates the sum of the gravity variation rate associated with PDIM (Table 8 in Sato et al. 2012), \dot{u}_e^{Sato} indicates the vertical deformation rate associated with the PDIM (Table 7 in Sato et al. 2012), and β_B indicates the Bouguer gravity gradient. When we use the value of -0.22 $\mu\text{Gal}/\text{mm}$ for β_B , \dot{g}_a^{Sato} is calculated to be -1.61 to

$+0.25$ $\mu\text{Gal}/\text{yr}$, which is negatively correlated with our calculation result, i.e., $\dot{g}_a^{UAF05} + \dot{g}_a^{UAF07}$ ($= -0.09$ to $+1.13$ $\mu\text{Gal}/\text{yr}$). In fact, if we correctly recalculate the total gravity variation rate of Sato et al. (2012) by reversing the sign of \dot{g}_a^{Sato} , the recalculated rate (diamonds in Fig. 9) is found to be consistent with our \dot{g}_{cal} (red circles) within 0.3 $\mu\text{Gal}/\text{yr}$ in the RMS.

Comparison with ground deformation data

To verify our rheological model in terms of ground deformation, we calculate the rate of vertical ground deformation (denoted by \dot{u}_{cal}) at each GNSS station in SE-AK using our rheological model, and compare it with the observed rate of vertical ground deformation (denoted by \dot{u}_{obs}). As for the observed deformation rate, we mainly used the results of the GNSS campaign observations conducted in the earlier studies (Larsen et al. 2004, 2005; Sato et al. 2011). We also downloaded the time series of three-dimensional coordinates observed at the other 11 continuous GNSS stations from websites of UNAVCO (Herring et al. 2016) or Nevada Geodetic Laboratory (Blewitt et al. 2018). We then determined the vertical deformation rate at each GNSS station by fitting the following function to the GNSS time series with the least-square adjustment:

$$f(t) = a_0 + a_v \cdot t + a_c \cdot \cos \frac{2\pi t}{T} + a_s \cdot \sin \frac{2\pi t}{T} + \sum_i^{n_{eq}} a_i \cdot H(t - t_i). \quad (14)$$

The coefficients of $(a_0, a_v, a_c, a_s, a_i)$, which are determined in the least-square adjustment, indicate the time-independent constant, the rate of time variation, the cosine and sine amplitudes of annual variation, and the step for earthquakes, respectively. In this equation, T , n_{eq} , $H(t)$ and t_i also indicate the time period of 1 year, the number of earthquakes, the Heaviside step function and the time when the i -th earthquake occurred, respectively. Figure 10d shows the vertical deformation rate observed at 99 GNSS stations in SE-AK (\dot{u}_{obs} ; a_v in the above equation), and the rate is greater than 0 mm/yr for almost all GNSS stations, and it is greatest ($+35.0$ mm/yr) at ANIT (Sato et al. 2011). Figure 10a also shows the histogram of the \dot{u}_{obs} 's distribution; the average and SD for \dot{u}_{obs} are obtained as $+17.47 \pm 8.17$ mm/yr (red and green lines).

The vertical deformation rate can be calculated using the same procedure as for calculating the gravity variation rate (Eqs. 4 and 10). The vertical ground deformation due to the past/present glacial melting (\dot{u}_v and \dot{u}_e , respectively) can be expressed by the following equations (e.g., Peltier 1974):

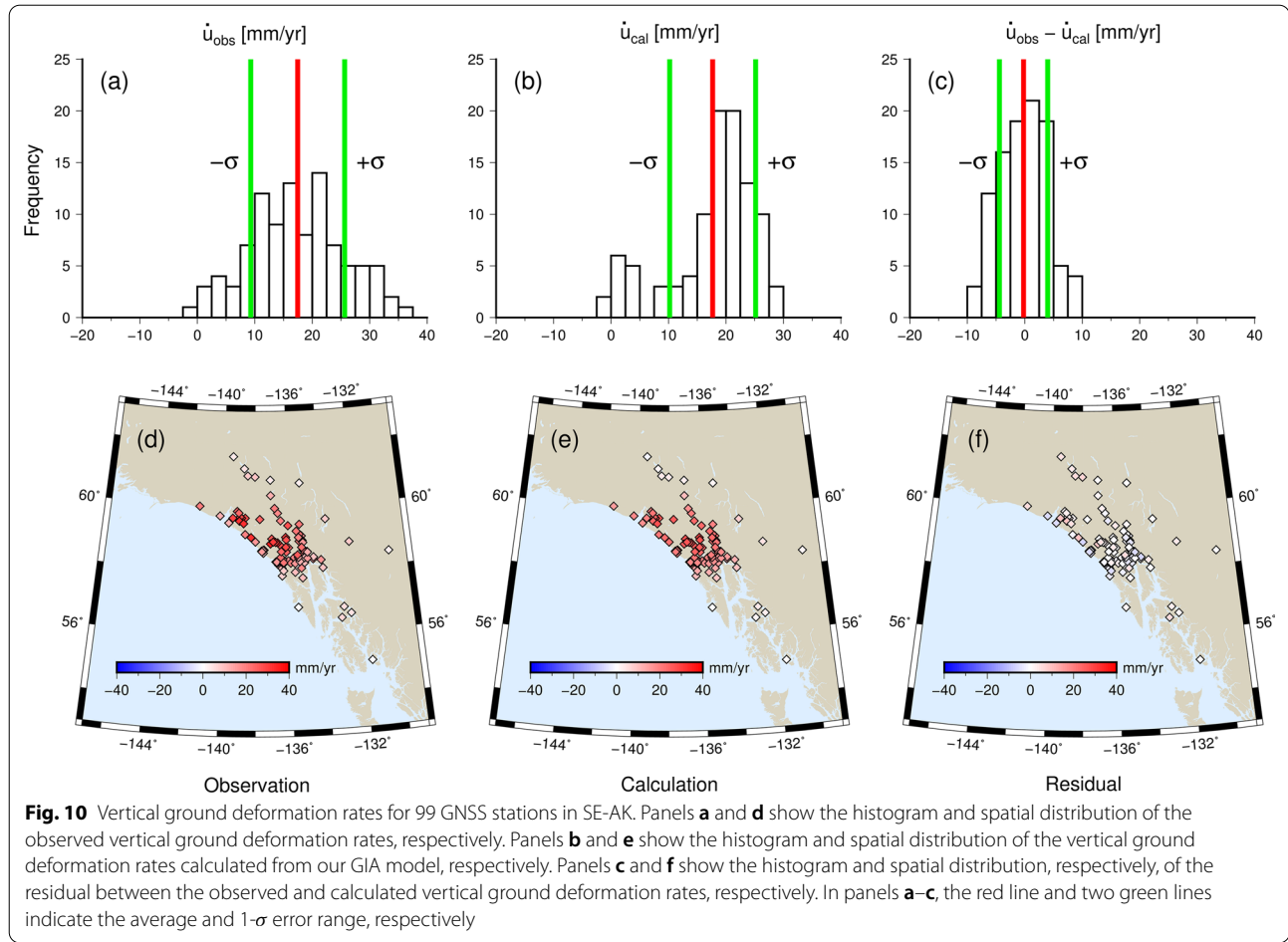


Fig. 10 Vertical ground deformation rates for 99 GNSS stations in SE-AK. Panels **a** and **d** show the histogram and spatial distribution of the observed vertical ground deformation rates, respectively. Panels **b** and **e** show the histogram and spatial distribution of the vertical ground deformation rates calculated from our GIA model, respectively. Panels **c** and **f** show the histogram and spatial distribution, respectively, of the residual between the observed and calculated vertical ground deformation rates, respectively. In panels **a–c**, the red line and two green lines indicate the average and $1\text{-}\sigma$ error range, respectively

$$\dot{u}_v(\phi_p, \lambda_p, t_0) = \rho_i \iint \Delta H_i(\phi, \lambda, s) \dot{G}_{uv}(\psi, t_0 - s) dS ds \quad (15)$$

$$\dot{G}_{uv}(\psi, t_0 - s) = \frac{R}{m_e} \sum_{n=0}^{n_{max}} \dot{h}_n(t_0 - s) P_n(\cos \psi) \quad (16)$$

$$\dot{u}_e(\phi_p, \lambda_p) = \rho_i \iint \dot{H}_i(\phi, \lambda) G_{ue}(\psi) dS, \quad (17)$$

$$\begin{aligned} \dot{u}_{cal} &= \dot{u}_v + \dot{u}_e \\ &= \left(\dot{u}_v^{GPIM} + \dot{u}_v^{RPIM} + \dot{u}_v^{LPIM} \right) + \dot{u}_e^{PDIM} \\ &= \left(\dot{u}_v^{GPIM} + \dot{u}_v^{RPIM} + \dot{u}_v^{LPIM} \right) + \left(\dot{u}_e^{LIAF07} + \dot{u}_e^{LIAF05} \right) \end{aligned} \quad (18)$$

where R and G_{ue} indicate the typical values of the radius of the Earth ($= 6378.1$ km) and elastic Green's function for vertical deformation due to point loading, respectively. We calculated the viscoelastic component (\dot{u}_v) using the time derivative of load Love number (\dot{h}_n ; Fig. 8) and the spatiotemporal variations of GPIM, RPIM and

LPIM. We also calculated the elastic component (\dot{u}_e) using the function G_{ue} expected from the 1066A Earth model (Gilbert and Dziewonski 1975; Matsumoto et al. 2001) and the spatial distributions of PDIM (composed of the UAF05 and UAF07 models). Figure 10e shows the sum of the calculated vertical deformation rates ($\dot{u}_{cal} = \dot{u}_e + \dot{u}_v$) at each GNSS station; \dot{u}_{cal} is large (up to $+29.50$ mm/yr) in Glacier Bay, and its distribution is similar to that of \dot{u}_{obs} (panel (d)). Figure 10b also shows the histogram of the \dot{u}_{cal} 's distribution; Its average and SD are calculated to be $+17.68 \pm 7.48$ mm/yr (red and green lines).

Figures 10c and f show the histogram and spatial distribution of the residual ($\dot{u}_{obs} - \dot{u}_{cal}$), respectively. The residuals are normally distributed within 10 mm/yr at all GNSS stations in SE-AK. Its average (-0.21 mm/yr) is almost equal to 0 mm/yr, and its SD (4.20 mm/yr) is about twice smaller than that of \dot{u}_{obs} (Fig. 10a). In these respects, the vertical ground deformation calculated from our rheological model agrees with that observed in SE-AK. Note that the average and SD of $\dot{u}_{obs} - \dot{u}_{cal}$ in our result are almost the same as those in Sato et al. (2011)

(-0.8 ± 3.3 mm/yr), although they obtained rheological parameters from the observed vertical deformation data directly. However, we succeeded in reproducing the deformation data using our rheological model, which was independently determined from the AG data.

Discussion

Ratio of gravity change to vertical displacement

The ratio of gravity variation to vertical ground deformation (\dot{g}/\dot{u}) have been discussed in earlier studies, associated with ice melting history and rheological structure, because the \dot{g}/\dot{u} value can be utilized for calculating gravity variation rate from uplift rate derived from GNSS data empirically. Wahr et al. (1995) found that the viscous part of \dot{g}/\dot{u} becomes a constant of about -0.154 $\mu\text{Gal}/\text{mm}$, based on numerical tests using a GIA model for Greenland and Antarctica. Olsson et al. (2015) also calculated the \dot{g}/\dot{u} values for three GIA regions (Laurentia, Fennoscandia and the British Isles) using several rheological models, and showed that the ratio differs more between the regions than between the earth models within each region. However, in the case of SE-AK, the characteristics of the ratio value have not been quantitatively discussed, mainly because both \dot{u} and \dot{g} include the elastic part owing to the PDIM, not only the viscoelastic part due to past ice melting. In fact, Sun et al. (2010) failed to isolate the elastic and viscoelastic parts from the \dot{g} values observed in SE-AK from 2006 to 2008, even though they utilized a quantity of $d\Delta/dt$ which is expected to

be independent of the viscoelastic effect (see Wahr et al. 1995). Therefore, we quantified the ratio values of gravity variation to vertical ground deformation in the SE-AK area using the observed/estimated values of \dot{u} and \dot{g} .

Figure 11a shows the raw ratio value, which is obtained as the observed gravity variation rate of the observed vertical deformation rate for each pair of the AG point and the continuous GNSS station (Table 1):

$$r_{raw}^{obs} = \frac{\dot{g}_{obs}}{\dot{u}_{obs}}. \quad (19)$$

The average and SD of r_{raw}^{obs} are -0.160 ± 0.030 $\mu\text{Gal}/\text{mm}$; r_{raw}^{obs} at some gravity points deviates from the average value, because the PDIM's attraction part contained in \dot{g}_{obs} differs between each gravity point.

Figure 11b shows the ratio value after the attraction effect was removed from the gravity variation rate. We refer to this ratio value as the total ratio (e.g., Olsson et al. 2015):

$$r_{tot}^{obs} = \frac{\dot{g}_{obs} - \dot{g}_a^{PDIM}}{\dot{u}_{obs}}, \quad (20)$$

$$r_{tot}^{cal} = \frac{\dot{g}_{cal} - \dot{g}_a^{PDIM}}{\dot{u}_{cal}}. \quad (21)$$

The observed total ratio (r_{tot}^{obs} ; green in Fig. 11b) averages to -0.173 $\mu\text{Gal}/\text{mm}$, which is greater (in absolute value) than the raw ratio (r_{raw}^{obs} ; Fig. 11a) by 0.013. The SD

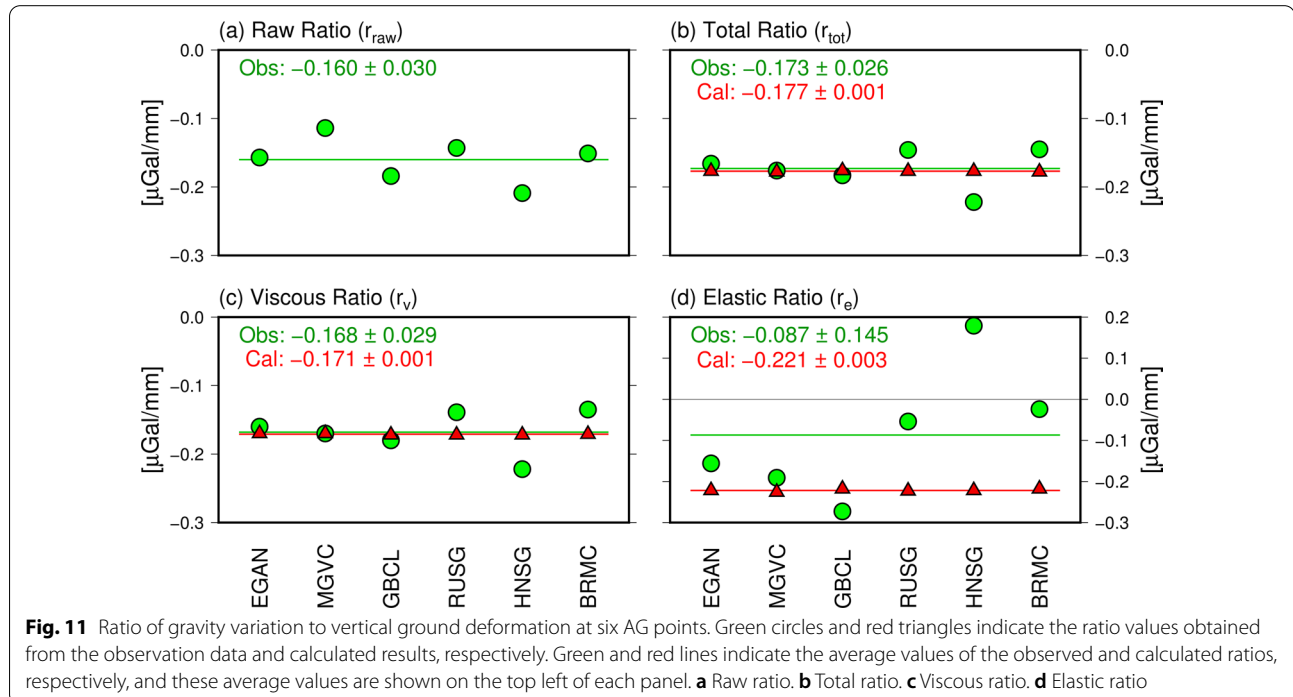


Fig. 11 Ratio of gravity variation to vertical ground deformation at six AG points. Green circles and red triangles indicate the ratio values obtained from the observation data and calculated results, respectively. Green and red lines indicate the average values of the observed and calculated ratios, respectively, and these average values are shown on the top left of each panel. **a** Raw ratio. **b** Total ratio. **c** Viscous ratio. **d** Elastic ratio

of r_{tot}^{obs} is smaller than that of r_{raw}^{obs} by 0.004; particularly, the deviation of the ratio value at MGVC from its average decreased from 0.046 (Fig. 11a) to 0.004 (Fig. 11b) by correcting for the PDIM attraction effect. Moreover, the calculated total ratio (r_{tot}^{cal} , red in Fig. 11b) was averaged to be $-0.177 \pm 0.001 \mu\text{Gal}/\text{mm}$, which is consistent with r_{tot}^{obs} within their error ranges. These results indicate that the attraction part due to the PDIM should be subtracted from the observed gravity data to obtain the \dot{g}/\dot{u} 's ratio associated with GIA accurately.

Figure 11c shows the viscous ratio value, i.e., the gravity variation rate to vertical deformation rate relating to past ice melting:

$$r_v^{obs} = \frac{\dot{g}_{obs} - \dot{g}_{ea}^{PDIM}}{\dot{u}_{obs} - \dot{u}_e^{PDIM}}, \quad (22)$$

$$r_v^{cal} = \frac{\dot{g}_{cal} - \dot{g}_{ea}^{PDIM}}{\dot{u}_{cal} - \dot{u}_e^{PDIM}} = \frac{\dot{g}_v^{GPIM} + \dot{g}_v^{RPIM} + \dot{g}_v^{LPIM}}{\dot{u}_v^{GPIM} + \dot{u}_v^{RPIM} + \dot{u}_v^{LPIM}}. \quad (23)$$

The observed viscous ratio (r_v^{obs} ; green in Fig. 11c) averages to $-0.168 \mu\text{Gal}/\text{mm}$, which agrees with the average of the calculated viscous ratio ($r_v^{cal} = -0.171 \mu\text{Gal}/\text{mm}$; red line in Fig. 11c) within their error ranges. The absolute value of the viscous ratio in SE-AK was larger than those in other GIA regions (-0.15 to $-0.16 \mu\text{Gal}/\text{mm}$; Wahr et al. 1995; Olsson et al. 2015), because the glacier has melted in SE-AK after LIA, which is more recent than in other regions. In fact, the Green's function for LPIM and RPIM indicates that the ratio value becomes greater (in absolute) for a younger melting event in the vicinity of a gravity point (see the range of $0 \leq \phi \leq 2$ deg in Fig. 8f).

Figure 11d shows the elastic ratio value, obtained as the gravity change to the vertical deformation associated with GIA due to PDIM only:

$$r_e^{obs} = \frac{\dot{g}_{obs} - \dot{g}_v - \dot{g}_a^{PDIM}}{\dot{u}_{obs} - \dot{u}_v}, \quad (24)$$

$$r_e^{cal} = \frac{\dot{g}_e^{PDIM}}{\dot{u}_e^{PDIM}}. \quad (25)$$

The observed elastic ratio (r_e^{obs} ; green in Fig. 11d) averages to $-0.087 \pm 0.145 \mu\text{Gal}/\text{mm}$, which significantly differs from the calculated elastic ratio ($r_e^{cal} = -0.222 \pm 0.003 \mu\text{Gal}/\text{mm}$; red in Fig. 11d). Particularly, r_e^{obs} at three AG points (RUSG, HNSG, and BRMC) largely deviate from r_e^{cal} , and the same characteristics can be seen for these AG points in the other panels (Fig. 11a–c). In the case of RUSG and BRMC, the cause of the inconsistency between r_e^{obs} and r_e^{cal} may be related to a systematic error in the observed gravity variation rate. As shown in

Fig. 9, \dot{g}_{obs} deviates from \dot{g}_{cal} more at RUSG and BRMC than at the other AG points, because the available AG data were fewer at RUSG and BRMC (Fig. 5), and hence, more AG data should be measured to determine the rate of gravity change more accurately. In the case of HNSG, the cause of the inconsistency between r_e^{obs} and r_e^{cal} may be due to the difference in location between the AG and GNSS points. We used the GNSS data collected at AB44 in Skagway (35 km north of HNSG in Haines), because no continuous GNSS station has been installed in Haines thus far. The installation of a continuous GNSS station around HNSG should be considered in a future study to compare ground displacement with gravity change directly. The observed elastic ratios at the other three AG points (EGAN, MGVC and GBCL) average to $-0.207 \pm 0.049 \mu\text{Gal}/\text{mm}$, which agrees with the average of r_e^{cal} within their error ranges.

The difference between r_v and r_e (Fig. 11c–d) can be explained mainly by the density value for each subsurface layer associated with GIA. In general, the ratio of the gravity variation to the vertical displacement can be approximately calculated by the Bouguer's gravity gradient:

$$\beta_B = \beta_F + 2\pi\rho G, \quad (26)$$

where the first and second terms indicate the free-air gradient ($= -0.3086 \mu\text{Gal}/\text{mm}$ as a typical value; Garland 1965) and the gravity change caused by a unit-thickness infinite plane with a density value of ρ , respectively. The viscoelastic part of the GIA can be interpreted as thickening of the upper-mantle thickness, and thus, the β_B value with a typical upper-mantle density of $3300 \text{ kg}/\text{m}^3$ is calculated to be $-0.17 \mu\text{Gal}/\text{mm}$, which is exactly consistent with r_v (Fig. 11c). In contrast, r_e^{cal} ($= -0.222 \mu\text{Gal}/\text{mm}$) is approximately 10% greater (in absolute) than β_B ($= -0.197 \mu\text{Gal}/\text{mm}$) when using a typical crustal density of $2670 \text{ kg}/\text{m}^3$ for ρ , because r_e^{cal} was calculated by considering the spatial variation in the medium density (see Farrell 1972).

The values of r_v^{cal} and r_e^{cal} may be utilized in separating the elastic/viscoelastic parts from the geodetic data acquired in SE-AK. If we assume that the attraction effect due to PDIM is negligible in the observed gravity change, the observed crustal deformation (\dot{u}_{obs}) and gravity change (\dot{g}_{obs}) can be written as (e.g., Sugawara 2011)

$$\dot{u}_{obs} = \dot{u}_v^{emp} + \dot{u}_e^{emp}, \quad (27)$$

$$\dot{g}_{obs} = \dot{g}_v^{emp} + \dot{g}_e^{emp} = r_v^{cal} \cdot \dot{u}_v^{emp} + r_e^{cal} \cdot \dot{u}_e^{emp}, \quad (28)$$

where each term with superscript *emp* indicates the value separated by this empirical method. When we substitute the observed values at GBCL (i.e., $+21.23 \text{ mm}/\text{yr}$ and $-3.92 \mu\text{Gal}/\text{yr}$) into these equations, \dot{u}_v^{emp} and \dot{u}_e^{emp} are

estimated to be +15.53 and +5.71 mm/yr, respectively, and the value of \dot{u}_v^{emp} agrees well with that obtained from our numerical calculation (= +18.87 mm/yr). However, in the case of MGVC, the value of \dot{u}_e^{emp} (= -20.28 mm/yr) differs from the calculation result ($r_v^{cal} = +2.08$ mm/yr) in terms of the sign and absolute value, because the attraction effect due to PDIM cannot be ignored at MGVC (Fig. 9). In these respects, this empirical method is valid only when the PDIM attraction effect is small.

The effect of acceleration in glacier melting

Earlier studies discussed the possibility of acceleration in glacier melting in the SE-AK region (e.g., Arendt et al. 2002). For example, Hu and Freymueller (2019) found that the rheological parameters for SE-AK were estimated differently if they used the GNSS time series observed in SE-AK during 1992–2003 or 2003–2012. They mentioned that the estimation results were distorted by the time variation in glacier melting rate during the analysis period from 1992 to 2012, and considered scale factors for a PDIM model (Berthier et al. 2010) so as to obtain the consistent rheological parameters regardless of analysis periods. The scale factors were calculated as 1.8 for 1992–2003 and 2.2 for 2003–2012, so they concluded that the recent PDIM rate duplicated relative to the PDIM model which is based on the ice elevation change from the 1960s to the 2000s (Berthier et al. 2010), and that the ice melting rate accelerated by approximately 20 % in and after 2003.

We here examine the dependence of the rheological parameters to the PDIM rate by changing a scale factor for the PDIM models (Arendt et al. 2002; Larsen et al. 2005, 2007) in the grid search calculation. Figure 12 shows the variations in the optimal parameters for (d, η) and their error ranges when we vary the scale factor for PDIM by 0.1 between 0.5 and 2.0. The optimal value of the lithospheric thickness (d ; red line) changed by just 3 km ($d = 54$ – 57 km) to the scale factor, and the optimal value of the upper mantle viscosity (η) with a 1.0's scale factor (the blue star) is located within the overall error range when the scale factor is varied from 0.5 to 2.0. In these respects, the model parameters were robustly determined in this study to be $d = 55$ km and $\eta = 1.2 \times 10^{19}$ Pa s (the stars in Fig. 12; see Fig. 7), as long as we used absolute gravity data (Fig. 5) for estimation of the model parameters. In fact, most of our AG points are insensitive to the PDIM effect, because the gravity change due to PDIM was calculated to be smaller than those due to LPIM and RPIM (Fig. 9). Although the PDIM effect was largest at MGVC (Mendenhall Glacier Visitor Center) in all of the AG points, the AG variation rate was obtained

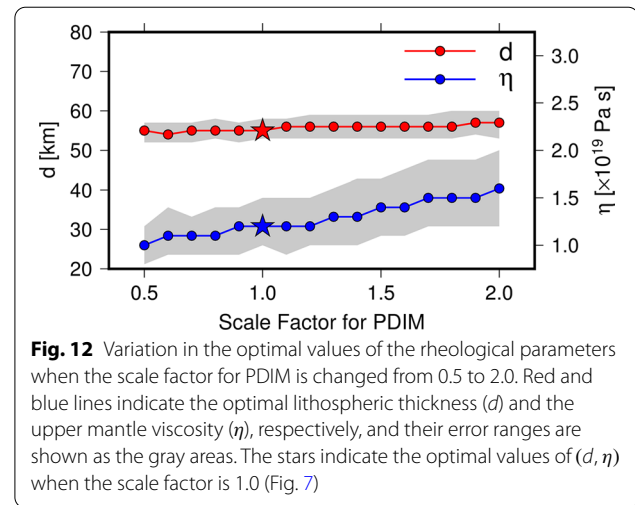


Fig. 12 Variation in the optimal values of the rheological parameters when the scale factor for PDIM is changed from 0.5 to 2.0. Red and blue lines indicate the optimal lithospheric thickness (d) and the upper mantle viscosity (η), respectively, and their error ranges are shown as the gray areas. The stars indicate the optimal values of (d, η) when the scale factor is 1.0 (Fig. 7)

with the lowest precision at MGVC (Fig. 5). Therefore, its weight was the smallest during our parameter estimation (Eq. 8). The scale factor for PDIM may be determined from the AG data directly if we repeatedly measure AG at MGVC with high accuracy in the future.

The upper mantle viscosity (η) slightly increases with an increase in the PDIM scale factor (Fig. 12) associated with the ice melting history in SE-AK as follows: when the PDIM scale factor is greater, the gravity variation rate due to PDIM (the green bars in Fig. 9) is also calculated to be greater in absolute value. The contributions of RPIM and LPIM (blue and cyan bars in Fig. 9, respectively) need to get smaller at most of the AG points to reconcile the sum of the ice-melting effects with the observed AG variation (red triangles and green circles in Fig. 9). Since RPIM and LPIM occurred in the SE-AK area after the end of the LIA in the 19–20th centuries (Larsen 2003; Larsen et al. 2005), which is more recent than GPIM, η 's increase leads to an increase in the time delay between the ice melting and the viscous ground uplift, and the resultant decrease in the present AG variation due to the RPIM and LPIM.

The effect of compressibility in estimating rheological parameters

We showed up to here that our rheological structure based on gravimetry well agreed with those based on GNSS data (Sato et al. 2011; Hu and Freymueller 2019). This study and previous studies calculated the GIA effects using the software of ALMA (Spada 2008) and TABOO (Spada 2003; Spada et al. 2003, 2004), respectively, which both assume the incompressible Earth. On the other hand, Tanaka et al. (2015) quantitatively investigated how much the Earth's compressibility affects the GIA response in the case of SE-AK. They showed from

numerical forward calculations that the GIA response (including vertical ground deformation and gravity change) in their compressible model became 27 % greater than that in the incompressible model (Spada 2003; Spada et al. 2003, 2004).

We here estimate the optimal rheological parameters (d and η) if using the compressible model, to quantify how much the optimal parameters can be biased by the presence or absence of compressibility in GIA models. According to the numerical calculations by Tanaka et al. (2015), the optimal parameters under the compressible Earth can be empirically estimated by enlarging the components of RPIM and LPIM by 1.27 times in calculating the χ^2 value (see Eqs. (8)–(9)). The green cross in Fig. 13 shows the the optimal combination of the rheological parameters (d and η) when the compressibility is empirically considered. In the compressible case, χ^2 reaches a minimum value of $\chi^2_{min} = 3.27$ at $d = 60$ km and $\eta = 1.6 \times 10^{19}$ Pa s. Although these values are within the ranges of our parameter values in the incompressible case ($47 \leq d \leq 64$ km and $0.5 \times 10^{19} \leq \eta \leq 2.0 \times 10^{19}$ Pa s; see the pink dashed lines in Fig. 13), the ranges of the 68.27 % confidence level (green and red ellipses) do not overlap with each other because of the existence of the negative correlation between d and η . The optimal values of d and η in the compressible case (green cross)

are 10 % and 25 % greater than those in our incompressible case (red cross), respectively, and this result is consistent with the implication by Tanaka et al. (2015) that the asthenospheric viscosity is underestimated by 27 % using the incompressible model.

We would like to claim here again that our rheological parameters were found to be consistent with those determined in the previous studies (Sato et al. 2011; Hu and Freymueller 2019) under the common assumption of the incompressible Earth. However, the optimal values of d and η obtained from the incompressible model can become smaller than those obtained from the compressible Earth, as described in this section. In future studies, more realistic Earth's models including compressibility need to be considered to determine rheological structures under SE-AK more accurately, and it will also contribute to a better understanding of GIA and PDIM in the vicinity of SE-AK.

Conclusions

To understand the spatiotemporal gravity variation associated with past and present ice melting, we measured the AG at six gravity points in SE-AK in 2012, 2013, and 2015, and reprocessed the new AG data in the common procedure with the past AG data obtained in 2006–2008 (Sun et al. 2010; Sato et al. 2012). After correcting the effects of hydrological and coseismic gravity changes from the reprocessed AG, we updated the gravity variation rate at the gravity points in SE-AK, using the AG time series from 2006 to 2015. The updated gravity variation rate ranged from $-2.05 \mu\text{Gal}/\text{yr}$ (at MGVC, the gravity point located in the Mendengall Glacier Visitor Center) to $-4.40 \mu\text{Gal}/\text{yr}$ (at RUSG, the gravity point located on Russell Island), and averaged to be $-3.25 \mu\text{Gal}/\text{yr}$. The standard deviation of the updated rate is much smaller than that in the previous study (Sun et al. 2010) at most of the gravity points, because our new AG measurements in 2012–2015 extended the data period from 3 years (Sun et al. 2010) to 10 years.

We then reproduced the observed AG variation rate, by numerically convolving the past/present-day ice melting models (Arendt et al. 2002; Larsen et al. 2004, 2005, 2007; Peltier et al. 2015) and Green's functions for viscoelastic/elastic loading deformations (Farrell 1972; Peltier 1974) under the assumption of the incompressible Earth. To reproduce the observed gravity variation rate, we searched for the optimal rheological parameters of the lithospheric thickness (d) and upper mantle viscosity (η) for the significant ice melting event that occurred in SE-AK at the end of the LIA. The optimal rheological parameters were determined to be $d = 55^{+9}_{-8}$ km and $\eta = (1.2^{+0.8}_{-0.7}) \times 10^{19}$ Pa s, which were both consistent with those obtained by earlier studies using GNSS data

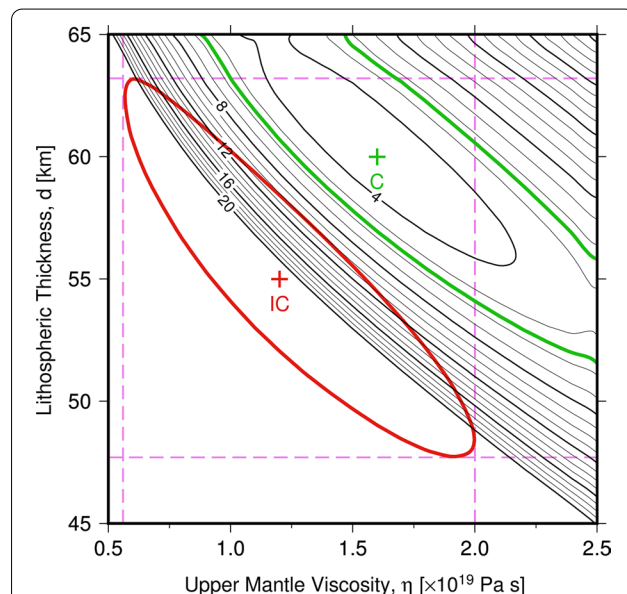


Fig. 13 Distribution of χ^2 to the variations of d and η in the compressible case. The green cross denoted by C indicates the position, where the χ^2 value reaches a minimum, and the green line indicates the 68.27 % confidence level of (η, d) . The red lines denoted by IC show the results obtained in this study by assuming the incompressible Earth (see Fig. 7), and pink dashed lines indicate the projection of its confidence level to each axis of d and η



Fig. 14 Location of the MGVC gravity point. **a** The satellite image of Mendenhall Glacier Visitor Center derived from Google Earth Pro. The red circle and green triangle indicate the MGVC gravity point and AB50 GNSS station, respectively. The white arrow indicates the direction of the photo **(b)**. **b** The entrance of Mendenhall Glacier Visitor Center. MGVC is located about 25 m from the entrance. **c** The elevator lobby of the Mendenhall Glacier Visitor Center, where the AG point is located. The new AG point is located on the right side of the lobby when facing the elevators. The old AG point (Sun et al. 2010) was located at the left side of the lobby. However, in June 2012, we found that the old point was not available because of the illuminating exhibition. The white arrow indicates the photo direction of Figure A5 in Sun et al. (2010). **d** The FG5-111 absolute gravimeter on the new AG point. **e** The position of the new AG point. It is located at the tip of the pen and approximately 109.5 cm from the corner of the heater. The heater should not be activated during the AG measurement, because its vibration magnifies the scatter of the AG data. **f** The exact position of the new AG point. It is located at the center of a tile and approximately 63.5 cm from the corner of the pillar. Note that we failed to measure the gravity difference between two AG points using a relative gravimeter directly during the campaign AG measurement in 2012, due to the exhibit installed on the old point by the visitor center. Instead, we considered the gravity difference by adding a term of the step-like gravity change between 2008 and 2012 in reproducing the temporal gravity change at MGVC (Fig. 5)

(Sato et al. 2011; Hu and Freymueller 2019) under the common assumption of the incompressible Earth. The error ranges of our optimal rheological parameters were as small as those in the most recent GNSS study (Hu and

Freymueller 2019); this result indicates that the rheological parameters under SE-AK can be precisely determined from the AG data, as well as from the GNSS data (e.g., Sato et al. 2011; Hu and Freymueller 2019). In addition,

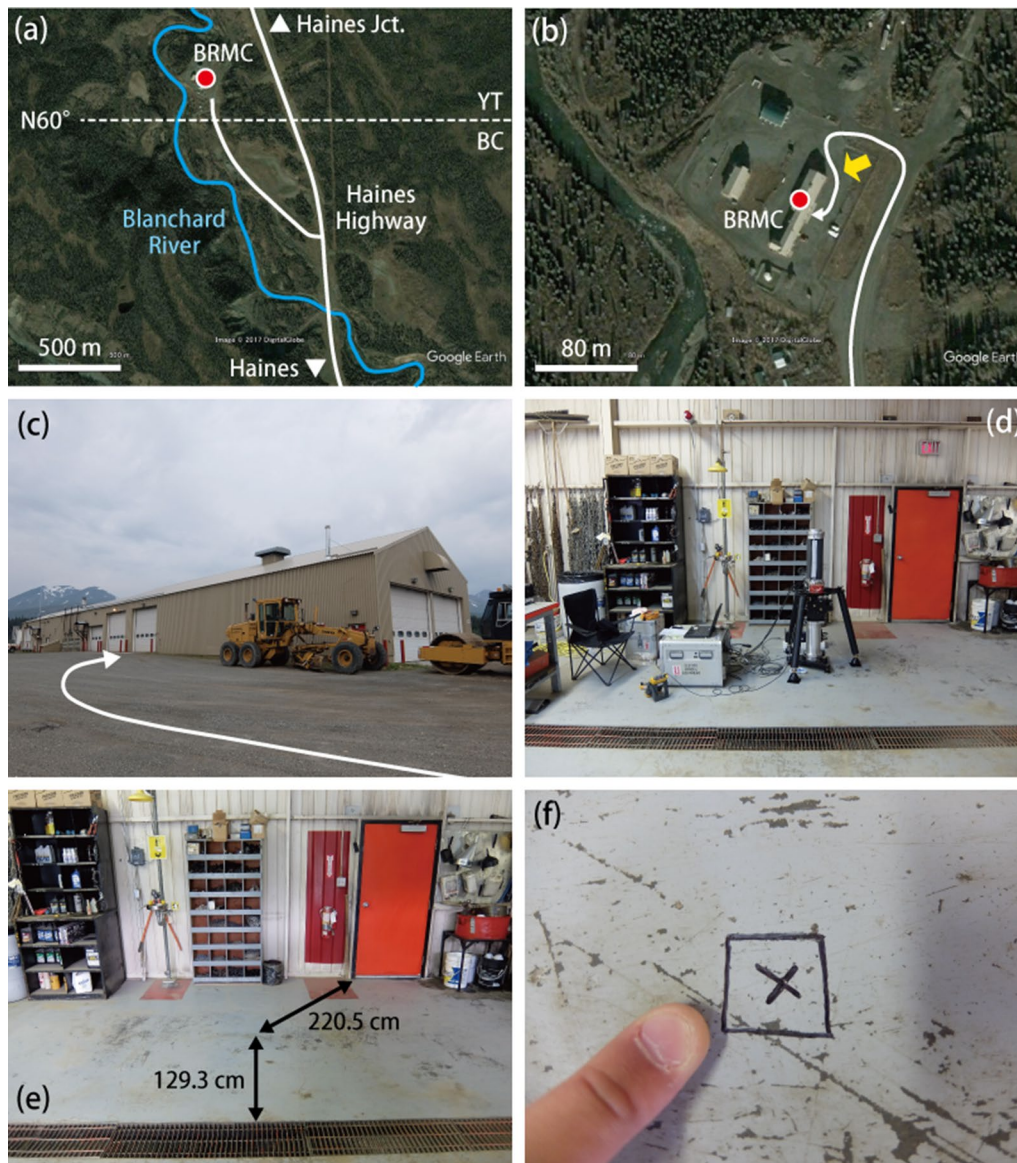


Fig. 15 Location of the BRMC gravity point. **a** Satellite image of the vicinity of BRMC derived from Google Earth Pro. The dashed line indicates the 60th parallel north, which corresponds to the border between the Yukon Territory (TY) and British Columbia (BC), Canada. When you access to BRMC (red circle), drive a van along the Haines Highway northward from Haines, and turn left after crossing over the Blanchard River. **b** Satellite image of BRMC derived from Google Earth Pro. The white line and yellow arrow indicate the access route to BRMC and the direction of the photo (**c**), respectively. BRMC (red circle) is located in the garage. **c** Garage of Blanchard Road Maintenance Compound. The white line indicates the access route to BRMC by car. The shutters at the tip of the white arrow can be opened when you transport AG instruments closely to the gravity point. **d** FG5-111 absolute gravimeter on the AG point. **e** Exact position of the AG point. It is located 129.3 cm from the corner of the gutter, and 220.5 cm from the corner of the red door. **f** Close-up photo of the AG point. This AG point was originally indicated with scratch marks of a small cross and a large square in and before 2012. However, the garage floor was painted by compound staff after the AG measurement in June 2012. Since we could not easily find the marks under the painting in June 2013, we highlighted the marks with a permanent marker for future AG measurements

the differences between observation and calculation were estimated to be $0.36 \mu\text{Gal}/\text{yr}$ for the AG time series and $0.21 \text{ mm}/\text{yr}$ for the GNSS time series, which are smaller than those in the earlier studies (e.g., Sato et al. 2011, 2012). In this respect, we succeeded in obtaining a robust

rheological model for SE-AK, which agrees with both of gravity and crustal deformation data.

We utilized the observed/calculated gravity variation rates to estimate the ratio of the AG variation to the vertical displacement at the gravity points in SE-AK.

The viscous ratio (r_v) was $-0.168 \mu\text{Gal}/\text{mm}$ from the observed data and $-0.171 \mu\text{Gal}/\text{mm}$ from the calculated result. These viscous ratio values for SE-AK are greater (in absolute) than those for other GIA regions (-0.15 to $-0.16 \mu\text{Gal}/\text{mm}$; Wahr et al. 1995; Olsson et al. 2015) because of the difference in the ice-melting history; significant mass of glacier melted in SE-AK after LIA, which is more recent than in the other regions. The elastic ratio (r_e) was also obtained as $-0.222 \mu\text{Gal}/\text{mm}$ from our numerical calculation. This value is greater (in absolute) than the typical Bouguer's gravity gradient ($-0.197 \mu\text{Gal}/\text{mm}$) due to the effect of the spatiotemporal variation in medium density (e.g., Farrell 1972).

We examined the dependence of the optimal rheological parameters to the PDIM rate by changing a scale factor for the PDIM models (e.g., Hu and Freymueller 2019). However, we found that the optimal parameters do not change with the variation in the scale factor. Specifically, the acceleration of PDIM cannot be confirmed from our AG data set (Table 2), because the gravity changes are only weakly sensitive to the PDIM component. Even though the MGVC gravity point is close to Mendenhall Glacier, our AG time series at MGVC is not sensitive to PDIM because of the large SD of the AG variation rate associated with the relocation the AG point between 2008 and 2012. To validate the acceleration of PDIM in the SE-AK region (Hu and Freymueller 2019) based on gravimetry, the temporal AG variation should be monitored at the six AG points by measuring the AG repeatedly in the future.

We finally examined how much the optimal rheological parameters can be biased by the presence or absence of compressibility in GIA models. The $\chi^2(\eta, d)$ value in the case of the compressible Earth was empirically calculated, based on the numerical results by Tanaka et al. (2015). The χ^2 value was found to reach a minimum at $d = 60 \text{ km}$ and $\eta = 1.6 \times 10^{19} \text{ Pa s}$; these optimal values are 10 % and 25 % greater than those in our incompressible case, respectively, although they are located within the error ranges of our optimal values. These results are consistent with the implication by Tanaka et al. (2015) that the incompressible model can underestimate the asthenospheric viscosity by 27 %. The Earth's compressibility should be considered for more accurate estimation of rheological structures under SE-AK in future studies, and it will also contribute to a better understanding of GIA and PDIM in the vicinity of SE-AK.

Appendix A. Description of absolute gravity points

Sun et al. (2010) described the detailed location of the following five AG points: EGAN (Egan Library, University of Alaska Southeast), MGVC (Mendenhall Glacier Visitor Center), GBCL (Gustavus Bartlett Cove), RUSG (Russell Island) and HNSG (Haines Fairground). In this appendix, we describe the detailed location of the MGVC gravity point (Fig. 14), because we compellingly relocated the gravity point in June 2012 due to an exhibit installed on the old gravity point by the visitor center. We also show the detailed location of BRMC (Blanchard Road Maintenance Compound) gravity point (Fig. 15), because earlier studies (Sun et al. 2010; Sato et al. 2012) did not describe its detailed location. Although Sun et al. (2010) did not collect any AG data at BRMC in June 2006, Sato et al. (2012) measured the AG at BRMC in June of 2007 and 2008 as part of the first ISEA project, and compared the AG with those obtained at the same gravity point in 1987 (Sasagawa et al. 1989).

Abbreviations

AG: absolute gravity; BP: before present; GIA: glacial isostatic adjustment; GNSS: Global Navigation Satellite System; GLDAS: Global Land Data Assimilation System; GPIM: global past ice melting; IERS: International Earth Rotation Service; ISEA: International Geodetic Measurements in Southeast Alaska; LIA: Little Ice Age; LPIM: local past ice melting; PDIM: present-day ice melting; PREM: Preliminary Reference Earth Model; RMS: root mean square; RPIM: regional past ice melting; SD: standard deviation; SE-AK: Southeast Alaska; SNOTEL: Snow Telemetry.

Acknowledgements

We are grateful to Tadahiro Sato (National Astronomical Observatory of Japan; Tohoku University), who passed away on 23 May 2021 at the age of 76, helped us measure AG in SE-AK and provided us with technical information to calculate the GIA response. We thank Max Kaufman (University of Alaska Fairbanks), Sam Herreid (Northumbria University), Kimberly DeGrandpre (Michigan State University), Yuning Fu (Bowling Green State University), and Gabrielle Vance (University of Alaska Southeast) for helping us measure the AG in SE-AK in 2012–2015. GMT (version 5.1.1) (Wessel et al. 2013) was used to create some figures in this study. The author Kazuhiro Naganawa received the Seto Prize of the Geodetic Society of Japan and this study was supported by the award.

Author Contributions

TK, SM, HH, and YO measured the AG in SE-AK from 2012 to 2015, and TK reprocessed the AG data collected from 2006 to 2015. KN analyzed the AG/GNSS data and constructed a GIA model for SE-AK. SM and JF provided overall supervision for this study, and YF provided technical advice for this study. KN drafted most of the manuscript, while TK drafted the manuscript of the section titled "Absolute gravity data". All authors read and approved the final manuscript.

Authors' information

KN and TK, Graduate School of Science, Kyoto University, Sakyo-ku, Kyoto 606-8502, Japan.

YF, Graduate School of Science, Kyoto University, Sakyo-ku, Kyoto 606-8502, Japan; Now at National Institute of Polar Research, Tachikawa, Tokyo 190-8518, Japan

SM and YO, Research Center for Prediction of Earthquakes and Volcanic Eruptions, Graduate School of Science, Tohoku University

HH, Institute for Cosmic Ray Research, the University of Tokyo, Kashiwa, Chiba 277-8582, Japan

JF, Geophysical Institute, University of Alaska Fairbanks, 2156 Koyukuk Drive, Fairbanks, AK 99775, USA; Now at Department of Earth and Environmental Sciences, Michigan State University, East Lansing, MI 48824, USA

Funding

This study was supported by JSPS KAKENHI Grant Numbers JP17253003 and JP23253003 from the Japanese Ministry of Education, Culture, Sports, Science and Technology.

Availability of data and materials

The SNOTEL snow accumulation data is provided by NRCS (<https://www.wcc.nrcs.usda.gov/snow/>). The Green's functions for elastic loading deformation based on the 1066A Earth model are available in the GOTIC2's software for computing oceanic tidal loading effects (Matsumoto et al. 2001; <https://www.miz.nao.ac.jp/staffs/nao99/>). The ETOPO1's digital elevation model is provided by NOAA (<https://www.ngdc.noaa.gov/mgg/global/>). The GLDAS-2.1's global hydrological model is provided by the NASA Goddard Earth Science Data and Information Services Center (<https://das.gsfc.nasa.gov/gldas/>). The slip distribution data of the Haida Gwaii and Craig Earthquakes (Lay et al. 2013) was provided by Thorne Lay (University of California Santa Cruz). The GNSS data sets are provided by UNAVCO (<https://www.unavco.org/data/gps-gnss/gps-gnss.html>) and Nevada Geodetic Laboratory (<http://geodesy.unr.edu/magnet.php>). The ICE6G_C's ice melting model and the VM5a's rheological structure are available from the web page of W. R. Peltier (<https://www.atmosp.physci.utoronto.ca/~peltier/data.php>). The ice melting models of RPIM, LPIM, and PDIM were provided by C. F. Larsen (University of Alaska Fairbanks), the corresponding author of the related articles (Larsen 2003; Larsen et al. 2004, 2005, 2007).

Declarations

Competing interests

The authors declare that they have no competing interests.

Author details

¹Graduate School of Science, Kyoto University, Sakyo-ku, Kyoto 606-8502, Japan. ²Present Address: National Institute of Polar Research, Tachikawa, Tokyo 190-8518, Japan. ³Research Center for Prediction of Earthquakes and Volcanic Eruptions, Graduate School of Science, Tohoku University, Aoba-ku, Sendai, Miyagi 980-8572, Japan. ⁴Institute for Cosmic Ray Research, the University of Tokyo, Kashiwa, Chiba 277-8582, Japan. ⁵Geophysical Institute, University of Alaska Fairbanks, 2156 Koyukuk Drive, Fairbanks, AK 99775, USA. ⁶Present Address: Department of Earth and Environmental Sciences, Michigan State University, East Lansing, MI 48824, USA.

Received: 15 December 2021 Accepted: 21 June 2022

Published online: 25 July 2022

References

- Amante C, Eakins B (2009) ETOPO1 1 arc-minute global relief model: procedures, data sources and analysis. NOAA technical memorandum NESDIS NGDC-24. National Geophysical Data Center, NOAA 10.5V5C8276M, 10.7289/V5C8276M
- Arendt AA, Echelmeyer KA, Harrison WD, Lingle CS, Valentine VB (2002) Rapid wastage of Alaska glaciers and their contribution to rising sea level. *Science* 297(5580):382–386. <https://doi.org/10.1126/science.1072497>
- Berthier E, Schiefer E, Clarke GK, Menounos B, Rémy F (2010) Contribution of Alaskan glaciers to sea-level rise derived from satellite imagery. *Nat Geosci* 3(2):92–95. <https://doi.org/10.1038/ngeo737>
- Blewitt G, Hammond WC, Kreemer C (2018) Harnessing the GPS data explosion for interdisciplinary science. *Eos* 99(10.1029):485. 10.1029/2018EO104623
- Dziewonski AM, Anderson DL (1981) Preliminary reference Earth model. *Phys Earth Planet Inter* 25(4):297–356. [https://doi.org/10.1016/0031-9201\(81\)90046-7](https://doi.org/10.1016/0031-9201(81)90046-7)
- Ekman M, Mäkinen J (1996) Recent postglacial rebound, gravity change and mantle flow in Fennoscandia. *Geophys J Int* 126(1):229–234. <https://doi.org/10.1111/j.1365-246X.1996.tb05281.x>
- Elliott JL, Larsen CF, Freymueller JT, Motyka RJ (2010) Tectonic block motion and glacial isostatic adjustment in southeast Alaska and adjacent Canada constrained by GPS measurements. *J Geophys Res Solid Earth*. <https://doi.org/10.1029/2009JB007139>
- Fang M, Hager BH (2001) Vertical deformation and absolute gravity. *Geophys J Int* 146(2):539–548. <https://doi.org/10.1046/j.0956-540x.2001.01483.x>
- Farrell W (1972) Deformation of the Earth by surface loads. *Rev Geophys* 10(3):761–797. <https://doi.org/10.1029/RG010i003p00761>
- Garland GD (1965) The earth's shape and gravity. Pergamon Press
- Gilbert F, Dziewonski AM (1975) An application of normal mode theory to the retrieval of structural parameters and source mechanisms from seismic spectra. *Philos Trans R Soc Lond Ser A Math Phys Sci* 278(1280):187–269. <https://doi.org/10.1098/rsta.1975.0025>
- Herring TA, Melbourne TI, Murray MH, Floyd MA, Szeliga WM, King RW, Phillips DA, Puskas CM, Santillan M, Wang L (2016) Plate boundary observatory and related networks: GPS data analysis methods and geodetic products. *Rev Geophys* 54(4):759–808. <https://doi.org/10.1002/2016RG000529x>
- Hu Y, Freymueller JT (2019) Geodetic observations of time-variable glacial isostatic adjustment in Southeast Alaska and its implications for Earth rheology. *J Geophys Res Solid Earth* 124(9):9870–9889. <https://doi.org/10.1029/2018JB017028>
- Huss M (2013) Density assumptions for converting geodetic glacier volume change to mass change. *Cryosphere* 7(3):877–887. <https://doi.org/10.5194/tc-7-877-2013>
- Inazu D, Sato T, Miura S, Ohta Y, Nakamura K, Fujimoto H, Larsen CF, Higuchi T (2009) Accurate ocean tide modeling in southeast Alaska and large tidal dissipation around Glacier Bay. *J Oceanogr* 65(3):335–347. <https://doi.org/10.1007/s10872-009-0031-y>
- James TS, Ivins ER (1998) Predictions of Antarctic crustal motions driven by present-day ice sheet evolution and by isostatic memory of the Last Glacial Maximum. *J Geophys Res Solid Earth* 103(B3):4993–5017. <https://doi.org/10.1029/97JB03539>
- Larsen CF (2003) Rapid uplift of southern Alaska caused by recent ice loss. PhD thesis, University of Alaska Fairbanks, <http://fairweather.alaska.edu/chris/thesis.pdf>, (Accessed on 30 June 2021)
- Larsen CF, Motyka RJ, Freymueller JT, Echelmeyer KA, Ivins ER (2004) Rapid uplift of southern Alaska caused by recent ice loss. *Geophys J Int* 158(3):1118–1133. <https://doi.org/10.1111/j.1365-246X.2004.02356.x>
- Larsen CF, Motyka RJ, Freymueller JT, Echelmeyer KA, Ivins ER (2005) Rapid viscoelastic uplift in southeast Alaska caused by post-Little Ice Age glacial retreat. *Earth Planet Sci Lett* 237(3–4):548–560. <https://doi.org/10.1016/j.epsl.2005.06.032>
- Larsen CF, Motyka RJ, Arendt AA, Echelmeyer KA, Geissler PE (2007) Glacier changes in southeast Alaska and northwest British Columbia and contribution to sea level rise. *J Geophys Res Earth Surface*. <https://doi.org/10.1029/2006JF000586>
- Lay T, Ye L, Kanamori H, Yamazaki Y, Cheung KF, Kwong K, Koper KD (2013) The October 28, 2012 Mw 7.8 Haida Gwaii underthrusting earthquake and tsunami: Slip partitioning along the Queen Charlotte Fault transpressional plate boundary. *Earth Planet Sci Lett* 375:57–70. <https://doi.org/10.1016/j.epsl.2013.05.005>
- Matsumoto K, Sato T, Takanezawa T, Ooe M (2001) GOTIC2: A program for computation of oceanic tidal loading effect. *J Geod Soc Jpn* 47(1):243–248. 10.11366/sokuchii1954.47.243
- Micro-g LaCoste (2006) FG5 absolute gravimeter user's manual. <http://microglacoste.com/pdf/FG5Manual2007.pdf>. Accessed 30 Jun 2021
- Micro-g LaCoste (2012) g9 user's manual. <http://microglacoste.com/pdf/g9Help.pdf>. Accessed 30 Jun 2021
- Nykolaishen L, Dragert H, Wang K, James TS, Schmidt M (2015) GPS observations of crustal deformation associated with the 2012 Mw 7.8 Haida Gwaii earthquake. *Bull Seismol Soc Am* 105(2B):1241–1252. <https://doi.org/10.1785/0120140177>
- Okubo S (1992) Gravity and potential changes due to shear and tensile faults in a half-space. *J Geophys Res Solid Earth* 97(B5):7137–7144. <https://doi.org/10.1029/92JB00178>

- Olsson PA, Milne G, Scherneck HG, Ågren J (2015) The relation between gravity rate of change and vertical displacement in previously glaciated areas. *J Geodyn* 83:76–84. <https://doi.org/10.1016/j.jog.2014.09.011>
- Peltier W (1974) The impulse response of a Maxwell Earth. *Rev Geophys* 12(4):649–669. <https://doi.org/10.1029/RG012i004p00649>
- Peltier WR, Argus D, Drummond R (2015) Space geodesy constrains ice age terminal deglaciation: the global ICE-6G_C (VM5a) model. *J Geophys Res Solid Earth* 120(1):450–487. <https://doi.org/10.1002/2014JB011176>
- Richards MA, Lenardic A (2018) The Cathles parameter (Ct): a geodynamic definition of the asthenosphere and implications for the nature of plate tectonics. *Geochem Geophys Geosyst* 19(12):4858–4875. <https://doi.org/10.1029/2018GC007664>
- Rodell M, Houser P, Jambor U, Gottschalck J, Mitchell K, Meng CJ, Arsenault K, Cosgrove B, Radakovich J, Bosilovich M et al (2004) The global land data assimilation system. *Bull Am Meteor Soc* 85(3):381–394. <https://doi.org/10.1175/BAMS-85-3-381>
- Sasagawa GS, Zumberge MA, Stevenson JM, Lautzenhiser T, Wirtz J, Ander ME (1989) The 1987 Southeastern Alaska gravity calibration range: absolute and relative gravity measurements. *J Geophys Res Solid Earth* 94(B6):7661–7666. <https://doi.org/10.1029/JB094iB06p07661>
- Sato T, Larsen CF, Miura S, Ohta Y, Fujimoto H, Sun W, Motyka RJ, Freymueller JT (2011) Reevaluation of the viscoelastic and elastic responses to the past and present-day ice changes in Southeast Alaska. *Tectonophysics* 511(3–4):79–88. <https://doi.org/10.1016/j.tecto.2010.05.009>
- Sato T, Miura S, Sun W, Sugano T, Freymueller JT, Larsen CF, Ohta Y, Fujimoto H, Inazu D, Motyka RJ (2012) Gravity and uplift rates observed in southeast Alaska and their comparison with GIA model predictions. *J Geophys Res Solid Earth*. <https://doi.org/10.1029/2011JB008485>
- Spada G (2003) The theory behind taboo. *Golden-White River Junction* 606
- Spada G (2008) ALMA, a Fortran program for computing the viscoelastic love numbers of a spherically symmetric planet. *Comput Geosci* 34(6):667–687. <https://doi.org/10.1016/j.cageo.2007.12.001>
- Spada G, Antonioli A, Boschi L, Brandi V, Cianetti S, Galvani G, Giunchi C, Perniola B, Agostinetti NP, Piersanti A, Stocchi P (2003) Taboo-user guide. *Golden-White River Junction*
- Spada G, Antonioli A, Boschi L, Brandi V, Cianetti S, Galvani G, Giunchi C, Perniola B, Agostinetti NP et al (2004). Modeling earth's post-glacial rebound. <https://doi.org/10.1029/2004EO060007>
- Sugawara Y (2011) Gravity measurements with the portable absolute gravimeter FG5 at Antarctica (IV). *Bull Geospat Info Auth Jpn* 121:9–19 (in Japanese)
- Sun W, Miura S, Sato T, Sugano T, Freymueller J, Kaufman M, Larsen C, Cross R, Inazu D (2010) Gravity measurements in southeastern Alaska reveal negative gravity rate of change caused by glacial isostatic adjustment. *J Geophys Res Solid Earth*. <https://doi.org/10.1029/2009JB007194>
- Tanaka Y, Sato T, Ohta Y, Miura S, Freymueller JT, Klemann V (2015) The effects of compressibility on the GIA in southeast Alaska. *J Geodyn* 84:55–61. <https://doi.org/10.1016/j.jog.2014.10.001>
- Timmen L, Wenzel HG (1995) Worldwide synthetic gravity tide parameters. In: *Gravity and geoid*, Springer, pp 92–101, https://doi.org/10.1007/978-3-642-79721-7_11
- Wahr J, DaZhong H, Trupin A (1995) Predictions of vertical uplift caused by changing polar ice volumes on a viscoelastic Earth. *Geophys Res Lett* 22(8):977–980. <https://doi.org/10.1029/94GL02840>
- Wessel P, Smith WH, Scharroo R, Luis J, Wobbe F (2013) Generic mapping tools: improved version released. *EOS Trans Am Geophys Union* 94(45):409–410

Publisher's Note

Springer Nature remains neutral with regard to jurisdictional claims in published maps and institutional affiliations.

Submit your manuscript to a SpringerOpen® journal and benefit from:

- Convenient online submission
- Rigorous peer review
- Open access: articles freely available online
- High visibility within the field
- Retaining the copyright to your article

Submit your next manuscript at ► [springeropen.com](https://www.springeropen.com)